Characterization of an optically readout gaseous time projection chamber with a ^{55}Fe source

Facoltà di Scienze Matematiche, Fisiche e Naturali
Corso di Laurea Magistrale in Fisica

Candidate
Donatella Tozzi
ID number 1661124

Thesis Advisors
Prof. Gianluca Cavoto
Dr. Davide Pinci

Co-Advisor
Dr. Giovanni Mazzitelli

Academic Year 2020/2021

Thesis defended on 19 January 2022
in front of a Board of Examiners composed by:

Prof. Antonio Davide Polosa (chairman)
Prof. Stefano Lupi
Prof. Stefano Giagu
Prof. Francesco Pannarale
Prof. Alessandro Paiella
Prof. Maria Chiara Angelini
Prof. Barbara Ruzicka
Dr. Francesco Pandolfi

Characterization of an optically readout gaseous time projection chamber with a ^{55}Fe source

Master's thesis. Sapienza – University of Rome

This thesis has been typeset by LaTeX and the Sapthesis class.

Version: August 4, 2022

Author's email: tozzi.1661124@studenti.uniroma1.it

Dedico questo traguardo ai miei genitori, che hanno sempre creduto in me, senza i quali non avrei avuto la possibilità di arrivare dove sono adesso; a mio fratello, che mi ha sempre sostenuto e supportato anche nei momenti più difficili regalandomi sorrisi indimenticabili; e all'uomo della mia vita, che dal primo momento ha creduto nel mio sogno più di me e senza il quale questo meraviglioso viaggio non sarebbe stato lo stesso.

Abstract

The nature of dark matter (DM) is currently one of the most intriguing questions of fundamental physics. Even if the question of dark matter finds its roots in astrophysics and cosmology, it is also actively searched for in particle physics experiments, at colliders as well as in dark matter detection experiments, which aim at discovering dark matter particles. The main experimental challenge comes of course from the elusive nature of DM. One of the most important observables connecting dark matter, cosmology and particle physics is the cosmological density of DM, which is called in this context the relic density.
In the last years, several experiments were performed to detect DM particles and some of these experiments use a direct directional detection of WIMP particles.
This thesis is an experimental thesis about the development of a new type of detector, called CYGNO. This detector is composed by a Time Projection Chamber filled with a gas mixture at atmospheric pressure. A triple GEM-system is used to produce the light in the detector. By using an optical readout the light is collected.
The thesis is composed by four chapters:

- **DARK MATTER:** in this chapter the evidence of Dark Matter in the Universe, the WIMPs candidates of DM, and the main Dark Matter experiments are described.
- **CYGNO experiment:** the CYGNO project is presented. In addition, in this chapter the different components of the detector used in the experiment are described.
- **The LIME prototype:** the LIME prototype and the experimental setup are described and the study of detector performances is presented: the response disuniformities and the response linearity.
- **Comparison with simulation:** in this chapter the comparison between data events and Monte Carlo events is discussed. The method of simulation is described and the study of response disuniformities and response linearity of data events and Monte Carlo events is presented.

Contents

Chapter 1

DARK MATTER

The nature of Dark Matter (DM) is currently one of the most intriguing questions of fundamental physics. Even if the question about the nature of DM finds its roots in astrophysics and cosmology, it is also actively searched for in particle physics experiments, at colliders as well as in DM detection experiments, which aim at discovering DM particles. The main experimental challenge comes of course from the elusive nature of DM. One of the most important observables connecting dark matter, cosmology and particle physics is the cosmological density of DM, which is called in this context the relic density.

1.1 Evidences of Dark Matter existence and its properties

A multitude of astrophysical and cosmological observations, involving different processes at diverse scales, provide evidence for the existence of non-baryonic Dark Matter in the Universe and in the halo of our Galaxy. These observations also provide hints to the properties of DM. Dark Matter makes up 27% of the total mass-energy density in the Universe. This precise measurement constrains the Dark Matter production mechanism in the early Universe and its interaction cross section. There are evidences for the existence of Dark Matter at different scales:

- **Galaxies:** One of the most striking evidences of unexpected gravitational effects comes from galaxies, and in particular spiral galaxies. In spiral galaxies most of the visible mass is gathered in the bulge and the disc. Using the Gauss' theorem, the velocity of stars v at the distance R from the galactic centre reads:

$$v(R) = \sqrt{\frac{GM(R)}{R}} \tag{1.1}$$

  where $M(R)$ is the total mass contained in a sphere of radius R. Far from the centre, the disc fades away, so that the star density decreases and the total mass inside the radius R becomes constant. As a consequence the velocity is expected to decrease as $v(R) \propto R^{-\frac{1}{2}}$. For most of spiral galaxies however the observed velocity far from the centre is approximately constant, leading to the so-called flat rotation curves of spiral galaxies. Considering a constant velocity v_0 within a radius R the mass inside this radius is given by:

$$M(R) = \frac{Rv_0^2}{G} \tag{1.2}$$

and the mass continues increasing far beyond the fading of the visible disc. In addition globular clusters around spiral galaxies are spread within spherical distributions around the galactic centres and extend well beyond the visible disc, constituting a spherical halo. Using a spherically symmetric distribution it is possible to show that the density leading to flat rotation curves reads:

$$\rho_M(R) = \frac{v_0^2}{4\pi G R^2} \tag{1.3}$$

corresponding to a decrease as R^{-2}, whereas the visible disc density decreases exponentially. Since most of the matter in the halo is invisible, its mass is considered to mainly come from Dark Matter. Similar results can be obtained when studying the dynamics of elliptical galaxies, and globally DM seems to represent about 80-90% of the total mass of galaxies.

- **Galaxy clusters:** Galaxy clusters are very massive objects which contain large quantities of gases in the intergalactic medium. These gases accelerated by the ambient gravity can reach high velocities and emit x-ray via Bremsstrahlung. During decades the analysis of the emitted x-ray together with a modelling of the galaxy clusters were used to weigh the total mass of the clusters, which was in turn compared to the visible mass. The results of such analyses were generally that a large fraction of the mass is invisible, but were often criticized for their approximate modelling. Such methods to determine the total mass of galaxy clusters have been superseded by gravitational lensing methods consisting in observing the deformed images of distant objects and reconstructing the path of the light which has been modified by the presence of masses affecting geometry locally. The most striking cases are the ones of strong gravitational lensing of distant galaxies behind a galaxy cluster, which appear under the form of several distorted images spread on the so-called Einstein circle. This effect is shown in the pictures 1.1a and 1.1b. The angular radius of the Einstein circle is related to the mass which gave rise to light deflection through the formula:

$$\theta_E = \sqrt{\frac{4MG}{c^2}\frac{(D_S - D_L)}{D_S D_L}} \tag{1.4}$$

where θ_E is the Einstein angular radius, M the mass of the lens, D_L the distance to the lens and D_S the distance to the source.
Gravitational lensing is therefore often used to weigh galaxy clusters, and numerous studies are consistent and tend to demonstrate that the visible mass represents only 10-20% of the total mass, similarly to the commonly found result in galaxies.

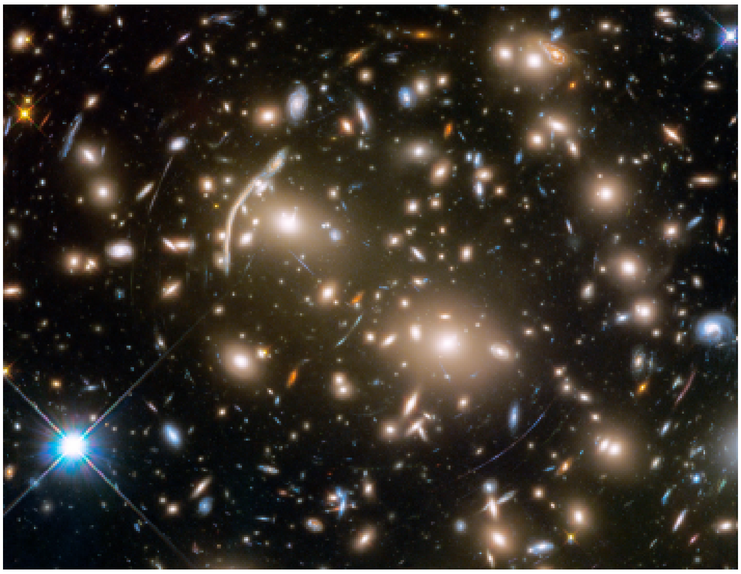

(a)

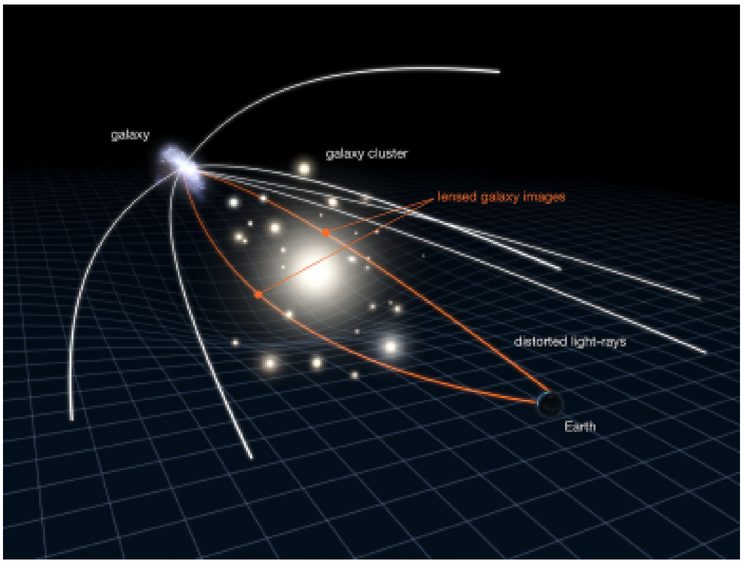

(b)

Figure 1.1. The picture 1.1a shows galaxy cluster Abell 370 composed of several hundreds of galaxies. The blue arcs are distorted images of remote galaxies behind the cluster. Credit: NASA, ESA, and J. Lotz and the HFF Team. The image 1.1b shows a schematic explanation of strong gravitational lensing by a cluster. Credit: NASA, ESA, and L. Calcada.

- **Large and cosmological scales:** The problem of DM extends to larger and cosmological scales. After recombination and emission of the CMB, atoms are formed and experience gravity as the main interaction. Matter starts gathering via gravitational collapse in the denser regions, forming large-scale structures in which galaxies also emerge. Two main effects affect structure formation: gravitational interaction attracts matter in the centres of masses, and the expansion of the Universe drives structures away from each other. Simulations of structure formation have been performed on supercomputers to study the interplay between expansion and gravity and study the role of Dark Matter in this process. In particular DM is generally considered as collisionless contrary to baryonic matter, so that it is possible to distinguish the role of DM from the one of baryonic matter in the simulations.

The observations reveal that Dark Matter is massive, stable over billions of years, very likely collisionless, interacting mostly gravitationally and separate from baryonic matter. If DM is made of new particles or objects, the first question is related to its thermal velocity. The terms "cold" and "hot" are used to characterize non-relativistic and relativistic speeds, respectively. Besides baryons, the only electromagnetically neutral, stable and massive particles that exist in the Standard Model (SM) are the neutrinos, which are so light that they have relativistic speeds and constitute a good example of hot Dark Matter. The important fact about hot DM is that, being composed of massive and high velocity components, it tends to spread structures such as galaxies, and if constituting the totality of Dark Matter, structures would be shaped very differently from what we observe, and the CMB anisotropies would have larger sizes. For this reason hot DM can constitute only a small part of total DM, and it is believed that most of DM is cold.
In the standard cosmological model it is assumed that dark matter and dark energy drive the expansion of the Universe today, and at the beginning of the Universe radiation was the dominant energy. The cosmological principle states that the energy distribution in the Universe is homogeneous and isotropic. Observations of the Universe have revealed that this principle is valid at large scales, whereas it is obviously not valid locally. This principle is the basis of the standard cosmological model. In terms of geometry, this is equivalent of considering that space is globally homogeneous and isotropic. The most general metric $g_{\mu\nu}$ which corresponds to these assumptions is the Robertson and Walker metric, which is written in terms of proper time as

$$d\tau^2 = g_{\mu\nu}dx^\mu dx^\nu = dt^2 - a^2(t)\left\{\frac{dr^2}{1-kr^2} + r^2(d\theta^2 + \sin^2\theta d\phi^2)\right\} \tag{1.5}$$

in a spherical coordinate system $x^\mu = (t, r, \theta, \phi)$, where $a(t)$ is the scale factor of the Universe which characterizes its expansion and is a function of the cosmological time t, and k is a global curvature which is the same at any point of the space-time. The cosmological principle implies that all quantities in the Universe are only dependent on time t and do not depend on position.
It is assumed that the different forms of energies in the Universe can be described as perfect fluids in adiabatic expansions with a total density $\rho = \sum \rho_{fluid}$ and pressure $P = \sum P_{fluid}$, leading to the stress-energy momentum tensor

$$T^{\mu\nu} = (P+\rho)U^\mu U^\nu - Pg^{\mu\nu} \tag{1.6}$$

where U^μ is the 4-velocity. In the rest frame of the cosmological fluids the nonzero components are $T^{00} = \rho$ and $T^{ij} = -Pg^{ij}$. For each of the fluids the energy conservation, which can be expressed as

$$D_\mu T^{\mu\nu}_{fluid} = 0 \tag{1.7}$$

where D_μ is the covariant derivative, leads to

$$\dot{\rho}_{fluid} + 3H(\rho_{fluid} * P_{fluid}) = 0 \quad (1.8)$$

The Hubble parameter H is defined as

$$H = \frac{\dot{a}}{a} \quad (1.9)$$

The Einstein equation leads to two independent equations:

$$H^2 = \frac{8\pi G}{3}\rho - \frac{k}{a^2} \quad (1.10)$$

$$\frac{\ddot{a}}{a} = -\frac{4\pi G}{3}(\rho + 3P) \quad (1.11)$$

where G is the Newton gravitational constant.
The values of the parameters at present time are denoted with a 0 index. In particular a_0 is the current value of the scale factor and we have:

$$H_0^2 = \frac{8\pi G}{3}\rho_0 - \frac{k}{a_0^2} = \frac{8\pi G}{3}\rho_0^c \quad (1.12)$$

where ρ_0^c is called "critical density" and H_0 is the "Hubble constant". The "critical density" discriminates the closed Universe from the opened one, that is, between the one determined by gravity (density greater than critical density) and that one dominated by expansion (density lower than critical density). The densities of different fluids are generally normalized by the critical density

$$\Omega_{fluid} = \frac{\rho_0^{fluid}}{\rho_0^c} \quad (1.13)$$

and the Ω_{fluid} densities are called "cosmological parameters".
The different fluids in the Universe are

- matter: made of a mixture of dark matter and baryonic matter
- radiation: composed of relativistic particle species such as photons and neutrinos
- dark energy: which is an unidentified component of negative pressure.

In the standard cosmological model, dark matter is considered as cold, i.e. with small velocities.
By convention, the beginning of the history of the Universe is set at $t = 0$, which corresponds to a scale factor $a(0) = 0$. It is however often considered that our physical description of nature is not valid before the Planck time $t_P = 5.39 \times 10^{-44}s$ where a quantum gravity description would be necessary. One generally considers the Planck time as the effective start time, when the scale factor was negligible. The total energy density is currently dominated by the cosmological constant, but from the observational values obtained by the Planck Collaboration [1] it results that matter was dominating in the recent past, whereas at the beginning of the

Universe radiation was dominating. Referring to the scale factor a to describe the past Universe, one generally refers to the redshift z such as

$$z = \frac{a_0}{a} - 1 \tag{1.14}$$

so that today corresponds to a zero redshift and the very beginning of the Universe to an infinite redshift. The Plank Collaboration deduced from the observational data the value of the redshift at which matter and radiation had equal densities:

$$z_{eq} = 3387 \pm 21 \tag{1.15}$$

which gives for radiation $\Omega_r \approx 9.2 \times 10^{-5}$. In terms of temperature, from statistical physics we have $\rho_r \propto T^4$, as long as the expansion is adiabatic. The temperature thus evolves as the inverse of the scale factor:

$$T \propto a^{-1} \tag{1.16}$$

In the standard cosmological model there are three main phases:

- a radiation domination era until $z \sim 3400$
- a matter domination era until $z \approx 0.3$
- a cosmological constant (co-)domination era at low redshift

Structure formation occurred mainly during the matter domination era and the cosmological constant thus started playing a role only very recently. The standard cosmological model offers a simple framework to study the evolution of the Universe, but it does not describe the other phenomena which may have occurred in the early Universe. The physics of the early Universe is indeed complicated, since the Universe went through different phases, in particular an inflation period during which the scale factor increased exponentially and also several phase transitions such as the electroweak phase transition. These periods are not observable directly, because the photons emitted during these phases were interacting too strongly with the plasma to carry information, and only after the formation of neutral atoms during the "recombination" period at a temperature of about 1 eV the photons can be considered as messengers which carry information. The photons emitted at the recombination time can still be observed today in the cosmic microwave background (CMB). The energetic photons emitted during recombination have had their wavelength redshifted and reduced by the expansion and are today observed in the microwave range corresponding to a temperature of 2.725 K. The CMB is an important vector of information, since its anisotropies and it is shown by the figure 1.2. Another indirect information about the early Universe comes from the abundance of the chemical elements. The nuclei have been formed during the so-called Big-Bang nucleosynthesis (BBN), by the combination of the nucleons. Models of BBN are considered as successfull and important tests of the Big-Bang model, and their predictions are in agreement with the observed abundances. During Big-Bang nucleosynthesis baryons combine to form complex nuclei.

At the beginning of BBN, i.e. a few seconds after the beginning of the Universe at a

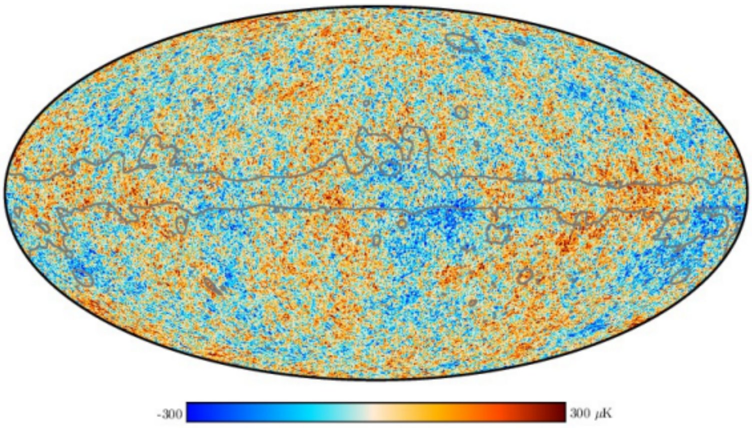

Figure 1.2. Full-sky map of the tiny temperature anisotropies over an average temperature of 2.725 K of the Cosmic Microwave Background. The grey contours show the position of the microwave emissions in the Milky Way and local structures.

redshift $z_{BBN} \sim 10^{11}$, the temperature was of the order of 100 MeV, or equivalently $10^{13}K$, and the cosmic plasma was made of photons, neutrinos, electrons and positrons in thermal equilibrium, and of baryons. The baryons had non-relativistic velocities and were not in thermal equilibrium. The densities of photons, neutrinos, electrons and positrons can be obtained from statistical physics considerations. The density of baryons is unknown, but the ratio of baryon number density to photon number density has been obtained from the CMB to be 6.09×10^{-10}. During BBN, the electrons and positrons annihilated, mainly into photons. As the expansion proceeded, the temperature decreased, thermal equilibrium was broken and the nuclei of the plasma interacted and formed heavier nuclei. BBN ended about 3 minutes after the beginning of the Universe at a temperature of about 10^9K.

1.2 The WIMP candidates and their interactions with standard matter

The fact that halos of Dark Matter surround galaxies and extend an order of magnitude in distance beyond the visible component of the galaxies implies that Dark Matter experiences at most weak dissipative interactions. Since estimates of the galaxies implies that the epoch of the CMB are consistent with present-day observations, DM must have a lifetime larger than Hubble time. The Hubble time is the time required for the Universe to expand to its present size, assuming that the Hubble constant has remained unchanged since the Big Bang. It is defined as the reciprocal of the Hubble constant, such as $1/\mathrm{H}_0$ [8]. Together these observations suggest that DM consists of at least one quasi-stable particle that is not part of the Standard Model of particle physics. One of the best motivated particle Dark Matter candidates is a stable, massive, neutral particle generally referred as a WIMP (Weakly Interacting Massive Particle). WIMPs are the main candidates of cold Dark

Matter.
WIMPs can interact with standard matter via scattering with nuclei of atoms. The probability of a WIMP-nuclear scatter that imparts a target nucleus with energy Q is the product of the WIMP-nuclear cross section $d\sigma_T/dQ$ and the velocity-weighted WIMP flux. This is integrated over all WIMP velocities $\vec{v}$ that are kinematically allowed to induce a nuclear recoil of energy Q. The minimum speed for this recoil, v_{min}, depends on the WIMP mass, the target nucleus mass m_T, the nuclear recoil energy Q, and the nature of the scatter. The general geometry of elastic scattering is

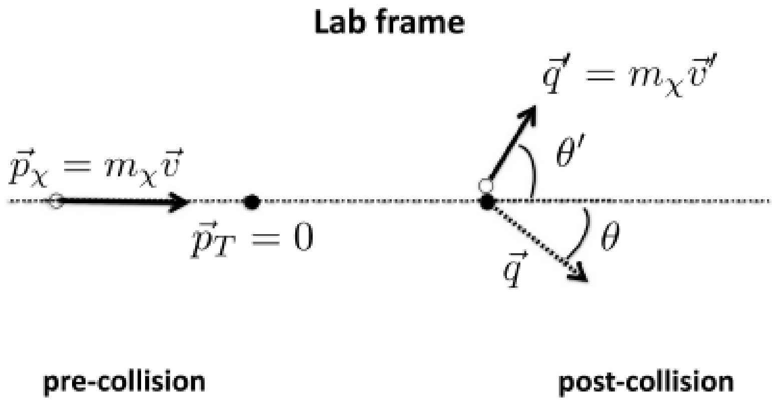

Figure 1.3. Kinematics of WIMP-nuclear elastic scattering. The open circle represents the WIMP, and the dark circle represents the target nucleus. The $\vec{p}'s$ and $\vec{q}'s$ represent momenta in the lab frame.

illustrated in figure 1.3. A WIMP with momentum $\vec{p} = m_\chi \vec{v}$ interacts with a nucleus at rest, inducing a nuclear recoil $\vec{q}$ with an angle θ with respect to the incoming WIMP direction. Thus, the lab-frame solid angle is $\Omega_q \equiv \hat{q} = (\theta, \phi)$, where the interactions are azimuthally symmetric around the WIMP incoming direction. The specific relationship between $\vec{q}$ and the incoming WIMP momentum depends on whether the WIMP-nuclear recoil is elastic or inelastic.
In elastic scattering the recoil energy depends smoothly on the center-of-mass frame scattering angle θ_{COM}

$$Q = \frac{\mu_T^2}{m_T} v^2 (1 - \cos\theta_{COM}) \tag{1.17}$$

and

$$v_{min} = \sqrt{m_T Q / 2\mu_T^2} \tag{1.18}$$

There are two primary ways in which Dark Matter and nuclei may experience inelastic interactions [2]. First, nuclei may transition to an excited state during interactions with WIMP particles. Second, DM may either be a composite particle or exist as part of a multiplet of dark states in a hidden-sector theory. If we consider the case in which DM belongs to a multiplet of dark states, these two states are labeled χ and χ^*, where the former is the lower energy state, and the latter is a higher energy state. The figure 1.4 shows this case. For inelastic Dark Matter (iDM) models, the DM is the lowest energy state χ. Interactions with nuclei cause a

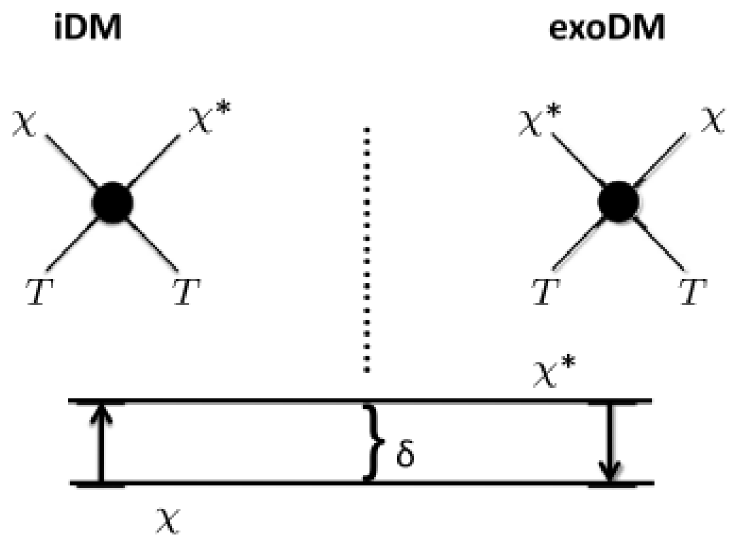

Figure 1.4. Inelastic dark matter. There are at least two dark-matter energy states, χ and χ^*, separated by energy δ. iDM models have χ as the DM, which may transition to χ^* through interactions with nuclei. exoDM models have χ^* as the DM, and may transition downward to χ by nuclear interactions.

transition to the χ^* state, which is an energy δ higher than the ground state. However in iDM transitions are forbidden for small initial WIMP kinetic energies and the minimum speed is

$$v_{min} = \frac{|m_T Q + \mu_T \delta|}{\mu\sqrt{2m_T Q}} \tag{1.19}$$

The inelastic interaction can happen the other way around: DM can be produced in an excited state in the dark multiplet χ^* and be down-scattered to the ground state χ through nuclear interactions. This kind of model is called exothermic Dark Matter (exoDM). By convention, one chooses to use $\delta > 0$ denoting iDM, and $\delta < 0$ denoting exoDM.

1.3 Principle of operations of Dark Matter detector

WIMPs with mass in the GeV to TeV range and speed $\sim 100\ \ km\ s^{-1}$ produce nuclear recoils with energy of order tens of keV. The expected event rates are also small, less than one event per kilogram target mass per year. To detect WIMPs a detector with low threshold energy, a large target mass and low background is required. The kinetic energy of the nuclear recoil can manifest itself as ionization, scintillation or phonons, leading to a rise in temperature. Electron and nuclear recoils deposit their energy between these channels differently. Therefore detectors which measure two channels can reject electron recoils efficiently. From a theorist's prospective, ongoing and near-future experiments can be classified by function instead of technology. The classification is as follow:

- experiments with little discriminating power on an event-by-event basis;
- experiments with discriminating power but no energy sensitivity above threshold;
- experiments with discriminating power and energy sensitivity;
- experiments with directional resolution for the nuclear recoil.

There exist two types of experiments with little discriminating power: scintillating crystals targets, and Germanium-diode experiments. With scintillating crystals, such as NaI and CsI, large detector arrays can be built. Pulse shape distribution can be used to allow discrimination between electron and nuclear recoils on a statistical, rather than event-by-event, basis.
There are currently some experiments using p-type point-contact germanium detector. They can distinguish events that occur in the bulk from those on the surface (a background) using pulse shapes.
In superheated droplet detectors, which are employed in the experiments with discriminating power but no energy sensitivity above threshold, the energy deposited by a nuclear recoil can trigger a transition to the gas phase, leading to the formation of bubbles which can be detected acoustically and optically.
The operating conditions, such as temperature and pressure, can be set so that only nuclear recoils, and not electron recoils, lead to bubble formation. Fluorine is a common target, and is particularly sensitive to spin-dependent interactions since most of its spin is carried by the unpaired proton.
The strong temperature dependence of the heat-capacity of dielectric crystals at low temperatures means that a relativity small energy deposit leads to a measurable rise in temperature and therefore cryogenic detectors operated at sub-Kelvin temperatures can measure the total recoil energy.
Combined with a measurement of, depending on the target material, either ionization or scintillation this allows discrimination between nuclear and electron recoils on an event by event basis. Cryogenic detectors also have low energy thresholds and excellent energy resolution.
For this reason they are employed in experiments with discriminating power and energy sensitivity. Large self-shielding detectors can be built using liquid noble elements. With liquid Argon (LAr) and Xenon (LXe) the simultaneous detection of scintillation and ionization allows event by event electron recoil discrimination.
Directional detection aims to measure both the energy and the direction of the recoiling nuclei. Constructing a detector capable of measuring the directions of sub-100 keV nuclear recoils is a difficult challenge. The directional detection strategy is based on the fact that the Sun is orbiting the Galactic centre and is currently travelling towards the constellation Cygnus.
If the WIMP distribution is predominantly smooth, the Sun's speed and the velocity dispersion of the WIMPs are expected to be similar in magnitude, and therefore the WIMP flux is concentrated around the direction of Solar motion.
The recoil track may be reconstructed either in 1D, 2D, or 3D, depending on the choice of the readout technology. Let $\vec{r}$ be the recoil direction given by

$$\vec{r} = \sin\theta\cos\phi\vec{x} + \sin\theta\sin\phi\vec{y} + \cos\theta\vec{z} \tag{1.20}$$

where the Earth-fixed $\vec{x}$, $\vec{y}$, and $\vec{z}$ axes point toward the North, the West and the Zenith directions respectively.
For 1D track reconstruction, the track is projected along the z-axis and hence the θ angle is measured. For a 2D track reconstruction, ϕ is measured, by projecting the track onto the (x, y) plane of the detector. A 3D track reconstruction requires that both the ϕ and θ angles are reconstructed.
Directional Time Projection Chambers (TPCs) are operated at low pressure so that the low energy recoil track is long enough to be detected on the readout plane. 3D track reconstruction can be achieved with a time-sampling of the 2D-projection of the ionization-induced electron cloud on a pixelized readout plane. 1D-directional detection could be achieved with liquid or even solid-state detectors. Low-pressure gas TPCs offer the best prospects for directional detection, and a number of prototype detectors are under development. This experimental thesis describes a DM detector which uses a gas TPC to detect the DM particles.

1.4 Main experiments and results

A large variety of underground experiments all over the world aim at the direct detection of the Milky Way halo's WIMPs. The main experiments are described below.

- DAMA/LIBRA: the DAMA/LIBRA experiments started its operation in 1990 at Gran Sasso underground laboratory (LNGS). The detector (DAMA) was initially based on nine 9.7 kg highly radio-pure NaI(Tl) scintillators shielded from radioactive background. The collaboration has then upgraded the detector to a sensitive mass of 250 kg of NaI(Tl). This new experiment, called LIBRA, is running since March 2003. The threshold for both the experiments is 2 keV and they are classified as experiments with little discriminating power on an event by event basis, as well as CoGeNT experiment.
  The DAMA experiment belongs to the first generation of Dark Matter direct detection experiments requiring a large detector exposure. Although the NaI(Tl) scintillator provides some discrimination between nuclear recoils and electronic recoils based on pulse shape, the collaboration published its data without any background reduction. The DAMA/LIBRA Collaboration combined the 290 kg $\times$ year exposure of DAMA with the 530 ton $\times$ year exposure of LIBRA, confirming in both cases a consistent modulation signal, as shown in figure 1.5. The modulation is the process of varying one or more properties of a periodic waveform, called the carrier signal, with a separate signal called the modulation signal that typically contains information to be transmitted. The total significance of the signal is 8.2σ.

- CoGeNT: the CoGeNT experiment is based on a 440 g, low threshold ($\sim 0.4\ keV$) P-type Point Contact (PPC) germanium detector. The PPC technology employed allows an effective surface background events rejection, thanks to the good position sensitivity. The detector is installed in the Soudan Underground Laboratory (SUL) and was operated from December 2009 to March 2011. During this period of operation it acquired 442 live-days of data for a

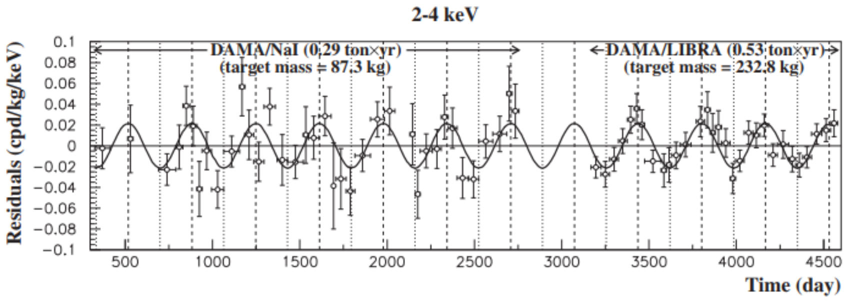

Figure 1.5. DAMA annual modulation signal from a model independent fit with the cosine function, showing a period of oscillation of 1.00 ± 0.01 year and offset t_0 equal to 140 ± 22 years.

total exposure of about 146 kg × day. The CoGeNT Collaboration reports an annual modulation signal, shown in picture 1.6, with a statistical significance of 2.8σ, with a modulation amplitude of $16.6 \pm 3.8\%$ mDRU, a period of 347 ± 29 days and the minimum occurring on Oct. $16 \pm 12d$.

- CRESST-II: the CRESST-II (Cryogenic Rare Event Search with Superconducting Thermometers) experiment is also located at the LNGS. This experiment is part of the experiments with discrimination power. CRESST-II is based on 9 scintillating $CaWO_4$ crystals of cylindrical shape, each with a mass of about 300 g. The crystals are operated as cryogenic calorimeters at temperatures of about 10 mK. The energy deposited by an interacting particle is mainly converted into phonons, which are detected with a Transition Edge Sensor (TES). A small fraction of the energy deposited in the crystal goes into scintillation light, which is detected by a cryogenic light detector. According to the different phonon to light yields ratio particles can be identified and background rejected. The Collaboration has published the results from the analysis of data collected between 2009 and 2011 (total net exposure of 730 kg × d), where the region of interest was defined in the energy interval $12 \div 40\ keV$. In article where the results of the analysis were published they stated that "Sixty-seven events are found in the acceptance region where a WIMP signal in the form of low energy nuclear recoils would be expected". With a maximum likelihood analysis they found that all the background sources are not sufficient to account for such a big excess of events. The figure 1.7 shows some results obtained from the analysis of data.

- XENON100: the XENON100 experiment exploits the time projection chamber (TPC) technology based on Liquid Xenon (LXe), with simultaneous detection of the ionization and the direct scintillation signals. The amplitude and timing of signals enables these TPCs to effectively reject background. The XENON100 experiment is installed at LNGS. The TPC sensitive volume is surrounded by an active liquid xenon veto. The total mass of Xe required to fill the detector is 161 kg, of which approximately 62 kg are in the target volume. By looking at the different light to charge yield ratio background events can be rejected. Moreover the double phase technique allows to further reduce the background

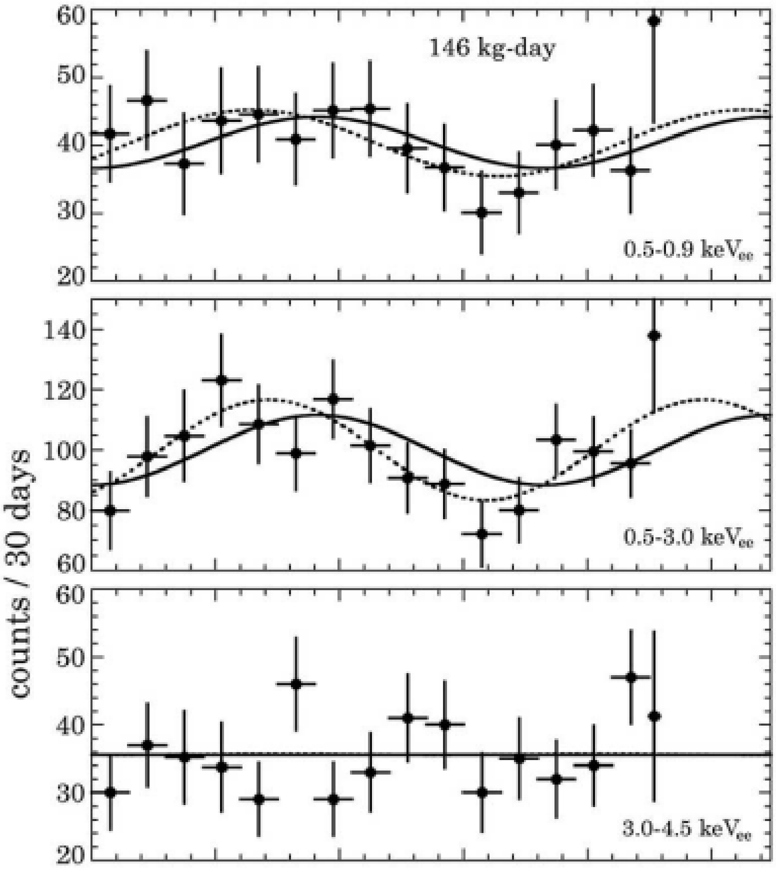

Figure 1.6. The picture shows CoGeNT data: rate *versus* time in several energy regions. The best-fit modulation is shown as a dashed line. The solid line indicates a prediction for a 7 GeV/c^2 WIMP in the galactic halo with a Maxwellian velocity distribution. The period of the modulation is compatible with the expected value from WIMPs in the galactic halo. No indication of a modulation is observed for the surface background events.

by applying fiducial volume cuts, such as exploiting the efficient self-shielding features of the LXe, and by single scatter selection criteria.
The collaboration has published the results of the analysis on a 224.6 live-days data sample acquired between February 2011 and March 2012 using a fiducial mass of 34 kg. Two candidate events were found in the signal region, where 1.0 ± 0.2 background events were expected. The results published are shown in pictures 1.8 and 1.9.

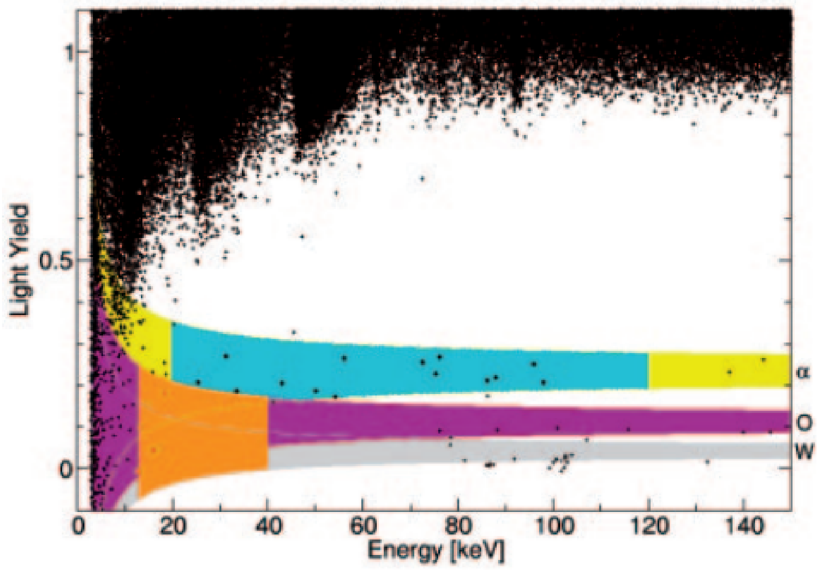

Figure 1.7. CRESST-II data of one crystal: light yield *versus* recoil energy. Electronic recoil events occur at high light yield (~ 1). The shaded areas represent the alpha, oxygen, and tungsten recoil bands. The acceptance region, the reference region in the α-band, and the events observed are also shown.

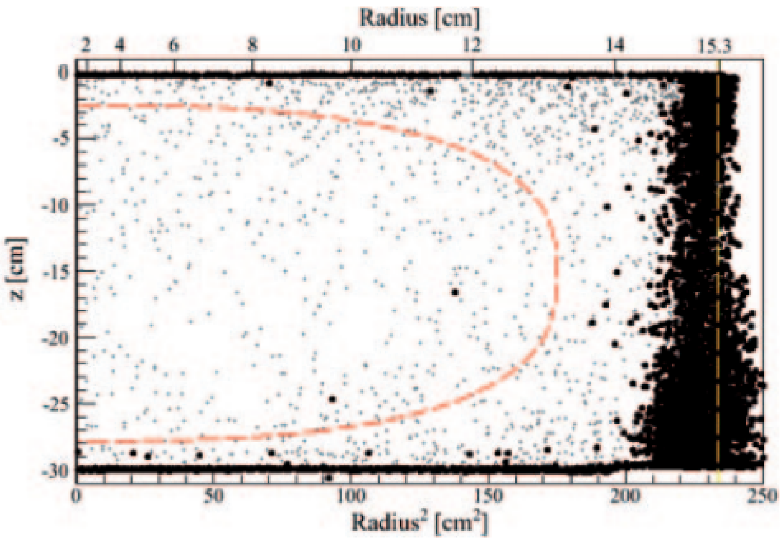

Figure 1.8. The figure shows the XENON100 data: 3D distribution of all the events (gray) and of the events below the 99.75% rejection (black dots) in the energy region of interest $(6.6 \div 30.5)$ keV_{nr}. The dashed line indicates the boundary of the 34 kg fiducial volume, while the gray line indicate the TPC dimensions. The two thicker dots falling inside the 34 kg fiducial volume indicate the two events found in the region of interest that pass all the analysis requirements.

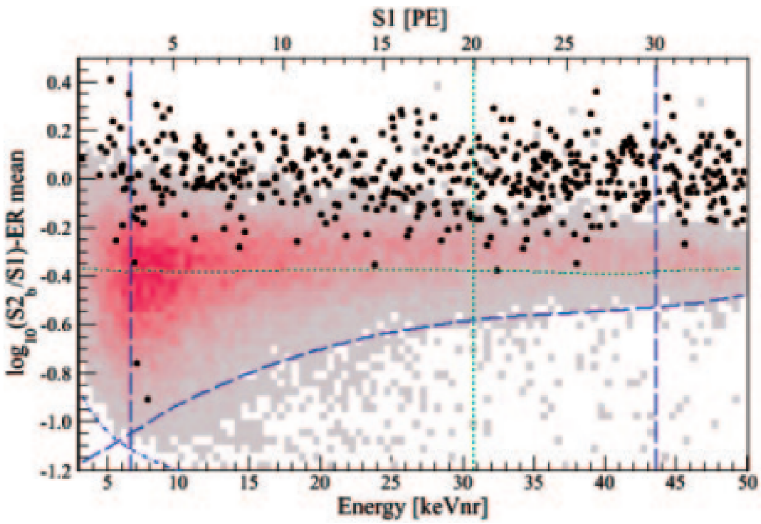

Figure 1.9. The figure shows the XENON100 data: flattened $log_{10}(S2_{bottom}/S1)$ versus nuclear recoil energy for all the events passing all the analysis requirements. The gray points indicate the nuclear recoil event distribution from a ^{241}AmBe calibration run. The dashed lines indicate the energy region selected for the final analysis, the software threshold $S2 > 300$ p.e, the 99.75% rejection line and the 3σ lower bound of the nuclear recoil band.

Chapter 2

CYGNO experiment

The CYGNO experiment (a CYGNus module with Optical readout) is part of the CYGNUS proto-collaboration [14] [15] which aims at constructing a network of underground observatories for directional DM search. This experiment is developing the new technique of the optical readout of a multi-GEM structure to exploit it in large volume TPCs for the study of rare events as interactions of low mass DM or solar neutrinos. The combined use of high-granularity sCMOS cameras and fast light sensors allows the reconstruction of the 3D direction of the tracks, offering good energy resolution and very high sensitivity in the few keV energy range, together with a very good particle identification useful for distinguishing nuclear recoils from electronic recoils. A one cubic meter demonstrator is expected to be built in 2022/23 aiming at a larger scale apparatus (30 m^3-100 m^3) at later stage.

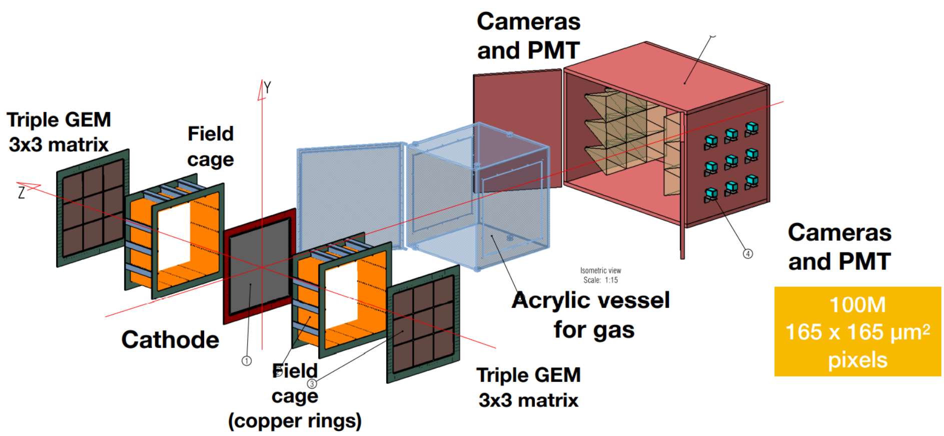

Figure 2.1. Drawing of 1-m^3 demonstrator. The TPC will be composed by two anodes composed by the triple-GEM system, and two field cages. At the centre of TPC a cathode is placed. The TPC will be insert in an acrylic gas vessel which will be placed in a box. At the ends of the box there will be the CMOS cameras and the PMTs.

The CYGNO project is composed by 3 phases:

- phase-0: which includes the underground installation of a 50-L prototype (LIME prototype);

- phase-1: which provides the 1-m^3 demonstrator;
- phase-2: that is the construction of a large scale experiment to search for rare events.

The phase-0 was anticipated by the construction of three prototypes (Orange, Lemon and LIME) and the study of their performances.

2.1 Time Projection Chamber

The CYGNO experiment goal is to deploy at LNGS a high resolution TPC with optical readout based on GEMs working with a helium/fluorine based gas mixture at atmospheric pressure for the study of rare events with energy releases in the range between hundreds of eV up to tens of keV.
PTCs usually comprise a sensitive volume, filled with gas or liquid, enclosed between an anode and a cathode generating a suitable electric field in it. The picture 2.2 shows an example of a generic TPC. The difference between the TPC shown in the figure 2.2 and that one used in CYGNO experiment is that in CYGNO the particles are born and die in the gas volume of the TPC.

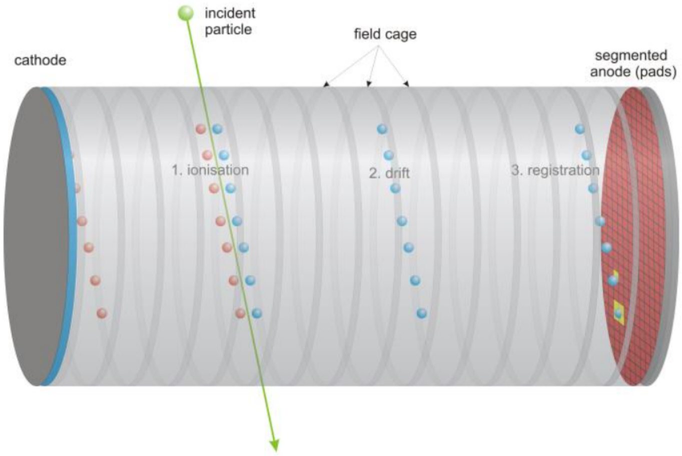

Figure 2.2. Example of working principle of a TPC. A charged particle crosses the gas volume and ionizes the atoms and molecules of gas. The ion-electron pairs drift towards the electrodes: the positive ions reach the cathode while the electrons drift towards the anode.

The passage of an ionising particle produces free electrons and ions that start to drift towards the above mentioned electrodes. These are usually segmented and read out to provide a granular information about the charge collection point on the plane. The third coordinate can be evaluated from the drift time measurements. On the contrary, in CYGNO experiment only relative times can be measured.
Therefore, TPCs are inherently 3D detectors capable of acquiring large sensitive volumes, with a lower amount of readout channels with respect to other high precision 3D tracking systems. Gaseous detectors can feature very low energy detection thresholds. In gas, a single electron cluster can be produced with energy releases of the order of few tens of eV and this has a very good chance of reaching

the multiplication region to produce a detectable signal.
TPCs can provide the best observable and architecture for a DM search experiment. The total ionization measured in a TPC indicates the energy of the recoil if the particle that crosses TPC stops in the gas volume. Comparison between track path and energy provides excellent identification of alphas and electrons. The track itself indicates the axis of the recoil and a measurement of the charge released along its path allows for inferring the sense of direction, providing the required directionality. The topological signature of the recoil event improves also particle identification and hence background rejection. TPCs energy threshold and angular performances are eventually determined by the gas composition and pressure, and by the granularity and noise to the signal ratio of the amplification and readout system. Gaseous TPCs constitute a promising approach to directional DM searches.
A large choice of gasses can be employed in TPCs, including light nuclei with odd number of nucleons (such as Fluorine), which are sensitive to both Spin-Independent (SI) and Spin-Dependent (SD) interactions also in the O(GeV) mass region. A room-temperature and atmospheric pressure detector results in operational and economical advantages, with no need for cooling or vacuum sealing. These choices allow for a more simpler technology and experimental realization and straightforward scaling when compared to cryogenic solutions currently dominating the DM direct search scene. The use of a gaseous target reduces the interaction probability with respect to denser material (liquid or solid). Nevertheless, TPCs up to 100 m^3 of active volume have already been successfully operated, and up nearly 20000 m^3 approved for construction in the neutrino field, showing the feasibility of very large detectors with large active masses.
Direct DM search detectors lack the magnetic fields that are typically present in TPC installed within experiments at colliders or beams and that can be used to control diffusion over long drift distances. In order to reduce the diffusion effects, a peculiar modification of the TPC operating principles has been developed within the DM field, called Negative Ion Drift (NID), with the DRIFT experiment pioneering this innovation.
With NID, primary electrons liberated by the track ionising the gas are captured at $O(\mu m)$ by the electronegative molecules, creating negative ions. The anions drift to the anode, where their additional electron is stripped and gives rise to a standard electron avalanche. Thanks to the anions mass being much larger than electrons, diffusion is reduced to the thermal limit with dispersion of O(1 mm/m), significantly improving tracking.

2.1.1 The diffusion effect

As the drifting electrons or ions are scattered on the gas molecules, their drift velocity deviates from the average owing to the random nature of the collisions. In the simplest case the deviation is the same in all directions, and a point-like cloud of electrons which then begins to drift at time t = 0 from the origin in the z direction will, after some time t, assume the following Gaussian density distribution:

$$n = \left(\frac{1}{\sqrt{4\pi Dt}}\right)^3 exp\left(\frac{-r^2}{4Dt}\right) \tag{2.1}$$

where $r^2 = x^2 + y^2 + (z - ut)^2$ and D is the diffusion constant because n satisfies the continuity equation for the conserved electron current Γ:

$$\Gamma = nu - D\nabla n \tag{2.2}$$

$$\frac{\partial n}{\partial t} + \nabla \cdot \Gamma = 0 \tag{2.3}$$

$$\frac{\partial n}{\partial t} + n\nabla \cdot u - D\nabla^2 n = 0 \tag{2.4}$$

The diffusion constant D , makes the mean squared deviation of the electrons equal to $2Dt$ in any one direction from their centre [9].
After a drift over a distance z, transverse and longitudinal profiles of electron clouds produced in these spots can be described by Gaussian curves with standard deviations that can be estimated as:

$$\sigma_T = \sqrt{\sigma_{T0}^2 + D_T^2 \cdot z} \tag{2.5}$$

$$\sigma_L = \sqrt{\sigma_{L0}^2 + D_L^2 \cdot z} \tag{2.6}$$

where σ_{T0} and σ_{L0} are constant contributions due to diffusion in the GEM structure and to channel pitch and D_T and D_L are transverse and longitudinal diffusion coefficients that depend on the gas mixture and electric field. In our case, we chose a z distance equal to 20 cm, $\sigma_{T0} = 350\ \mu m$, $\sigma_T = 0.11\ mm/\sqrt{cm}$, $\sigma_{L0} = 260\ \mu m$ and $\sigma_L = 0.099\ mm/\sqrt{cm}$.

2.2 Gas Electron Multipliers

The Gas Electron Multiplier (GEM) is a micro-pattern gas detector that can be used for the high resolution particle tracking. The standard GEM is a kapton foil with a thickness of about 50 μm, clad on each side with a thin copper layer (5 μm) and perforated with holes with a high surface density. The holes have a bi-conical shape with a diameter ranging from 50 μm to 70 μm. The pictures 2.3 and 2.4 show a foil magnification and the hole cross-section respectively, seen at electron microscope. By means of this device the electrons produced in a gas mixture by a ionizing particle are multiplied within the GEM channels where a high electric field is present.

It is possible to produce within the holes an electric field of 100 kV/cm,called channel field E_c, by applying a voltage difference of about 500 V between the two copper sides. When a charged particle passes through the gas, ionizes molecules that generate primary electrons. An external electric field, the drift field E_d, brings the primary electrons through the GEM and the high field inside the holes induces an avalanche process. In the transfer gap a transfer electric field E_t extracts secondary electrons. The pictures 2.5a and 2.5b show the equipotential lines around the channel and the electron drift lines without diffusion effect.

Because of the diffusion effect and the defocused field lines, the electrons can collide with the upper GEM electrode, as the picture 2.6 shows. The ratio between the number of electrons entering in the channel and the number of electrons which reach the upper side of the GEM is defined as the collection efficiency: ϵ_{coll}^{el}.

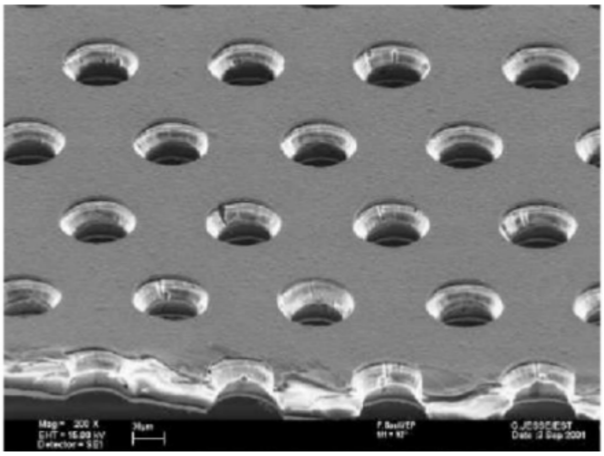

Figure 2.3. GEM foil seen under the electron microscope. It is possible to see the high surface density of channels.

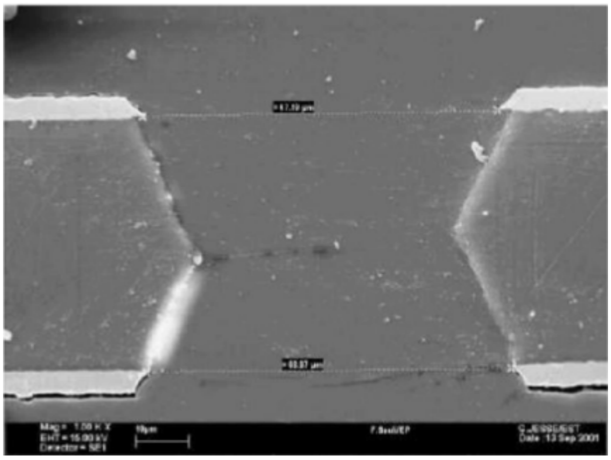

Figure 2.4. GEM hole cross-section seen at electron microscope. The GEM foil is composed by bi-conical holes with an external diameter of 70 μm, an internal diameter of 50 μm, and a pitch of 140 μm.

Some electrons are lost on the kapton inside the GEM while others can hit the lower side of the GEM foil due to the poor extraction capability of the electric field below the GEM. The ration between the number of electrons extracted and the number of electrons entering in the channel is the extraction efficiency: ϵ^{el}_{extr}. The probability that an electron produced in the drift zone arrives in the transfer area crossing a channel of the GEM foil is called electron transparency. The electron transparency is a decisive parameter for the energy resolution and directly affects the detection performance and it is defined as

$$T = \epsilon^{el}_{coll} \cdot \epsilon^{el}_{extr} \tag{2.7}$$

When the electric field E_d increases a large fraction of electrons can hit the upper GEM copper side causing the decrease of the electron transparency. On the other hand a high electric drift field is necessary to avoid charge losses in the gas through

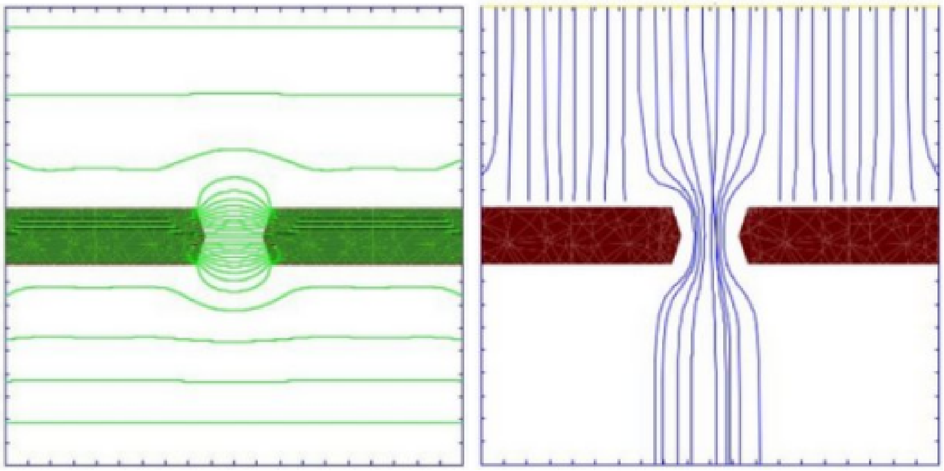

(a) Equipotential lines around the GEM channel.

(b) Electron drift lines without diffusion effect. Some drift lines reach the upper side of GEM foil, while other lines pass through the GEM channel.

Figure 2.5. Region of $400 \times 400\ \mu m$ around the GEM channel.

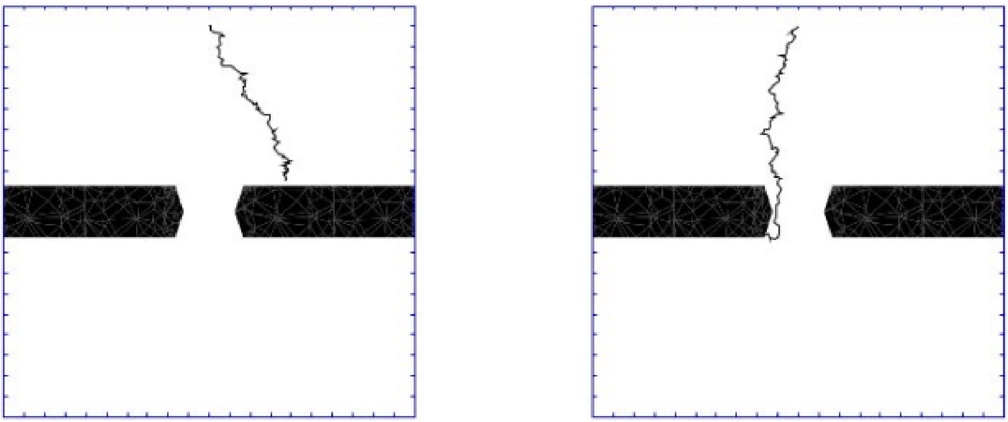

Figure 2.6. Example of simulated processes. On the left, electron hitting the upper electrode, on the right, electron lost inside a GEM channel.

secondary effects, as the recombination. In the figure 2.7 the dependence of the efficiencies on the two electric fields (drift and transfer) is shown.

The ϵ_{coll}^{el} and the transparency decrease at high drift fields due to the defocusing effect while with a better electron extraction capability the total transparency of the GEM increases at high transfer fields.
When the particle crossing the gas volume of the detector has an energy that exceed the first ionization potential of the gas molecules, the ion-electron pair production occurs which is the first step of the avalanche multiplication. The number of pairs

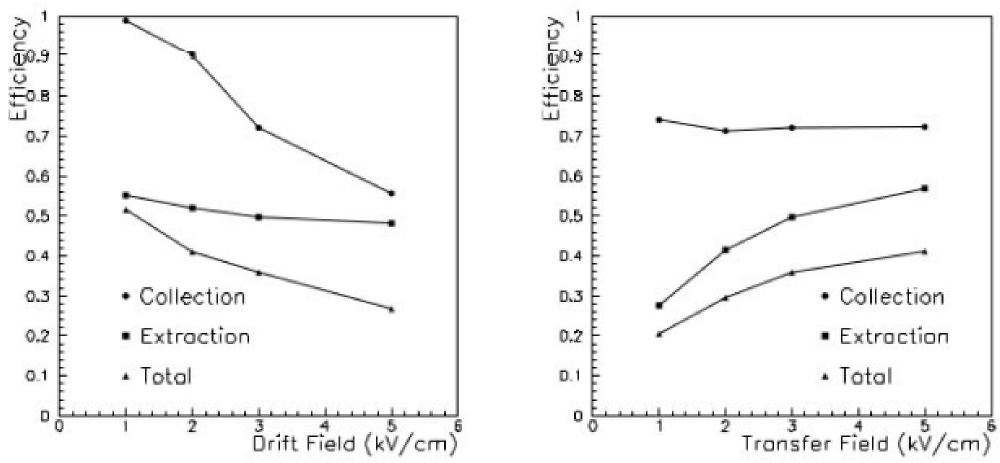

Figure 2.7. Transparency dependence on drift field (plot on the left), and transfer field (plot on the right).By looking the plot on the left, we can note that ϵ_{coll}^{el} decreases as the drift field increases, ϵ_{extr}^{el} assumes an almost constant trend, and the transparency (total) follows the trend of ϵ_{coll}^{el}. By looking the image on the right, ϵ_{coll}^{el} is constant as the transfer field changes, ϵ_{extr}^{el} increases with the increase of the transfer field, and the transparency (total) assumes the same trend of ϵ_{extr}^{el}.

produced in a dx path is linearly proportional to the number of electrons:

$$\frac{dn}{dx} = \alpha(E) \cdot n \tag{2.8}$$

The $\alpha(E)$ is called first Townsend coefficient and it is a function of the electric field. The electric field in the channel E_c allows the development of the avalanche: the number of secondary created by primary electrons increases with the increase of E_c, but it reduces the extraction of the secondary electrons affecting the transparency. If electronegative gases are used, the electron capture process will occur. The associated equation will be:

$$\frac{dn}{dx} = -\eta(E) \cdot n \tag{2.9}$$

where $\eta(E)$ is called attachment coefficient.
The gain for a single electron going from x_1 to x_2 resulting from the above equation is:

$$G_{single} = exp(\int_{x_1}^{x_2} [\alpha(E) - \eta(E)]dx) \tag{2.10}$$

It takes into account two effects: if the field in the channel is sufficiently high the attachment effect can be neglected with respect to the multiplication; the drift lines are concentrated near the channel axis. Due to the diffusion effect the electrons can reach the regions close to the kapton where the higher field results in higher multiplication.
The average number of secondary electrons produced per single electron entering into a hole is indicated as intrinsic gain G_{intr} while the average number of secondary electrons extracted from the lower side of GEM per primary electron generated

above the GEM is indicated as efficiency gain G:

$$G = G_{intr} \cdot T \tag{2.11}$$

2.2.1 The Triple-GEM

A triple-GEM detector is a device composed by 3 GEM foils inserted between two conductive planes: the cathode which forms the drift gap above the first GEM, and the anode which is usually used as signal readout. The ionization of the gas molecules occurs in the drift gap, the space between the cathode and the first GEM. The regions between the GEM are called transfer gaps while the induction gap is the gap between the last GEM and the anode, as the picture 2.8 shows.

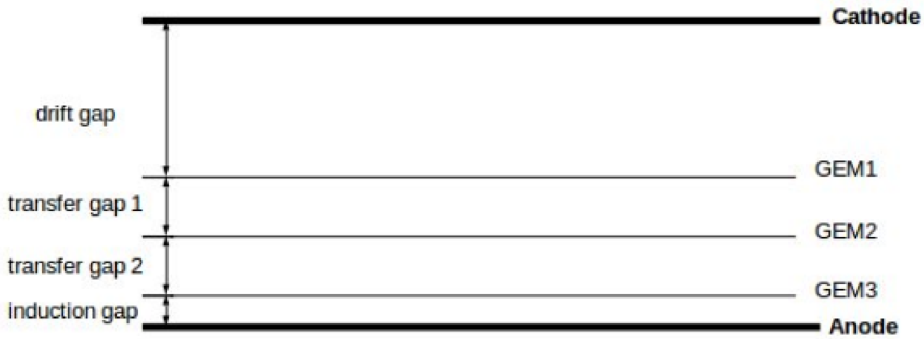

Figure 2.8. Schematic view of the triple-GEM system. The GEM1 foil is placed between the drift gap and the first transfer gap, the GEM2 is between the two transfer gaps, and the GEM3 is placed between the second transfer gap and the induction gap. In CYGNO experiment the drift gap corresponds to the total volume of the detector.

Electrons produced in the ionization process reach the first GEM by means of the drift electric field, and then by means of two transfer electric fields the electron clouds reach the second and the third GEM. Once the electrons cross the last GEM and reach the induction gap they give rise to the formation of an induced current signal on the anode. This current is amplified and shaped by the readout electronics. In the case of CYGNO experiment the induction gap is not present since there is no a further electrode after the GEM structure which acts as an anode. For this reason we only read the current on the single GEM.

In the transfer gaps, the secondary electron clouds are carried out from the first GEM and drifted towards the following one. Therefore, the electric field in the transfer gap (E_t) is an important parameter to be studied and optimized. In order to ensure a good extraction capability of the secondary electrons from the upper GEM in the transfer gap a high E_t is required. On the other hand E_t has to be jet low to reduce the defocusing effect.

Each single GEM has an effective gain which is an exponential function of the voltage applied:

$$G^{(i)} = A_k e^{\alpha_k V^i_{gem}} T_{(i)} \tag{2.12}$$

A_k and α_k depend on the gas mixture and T depends on the field above and below the GEM.
For a system with three GEM sandwiched the gain is essentially given by:

$$G = G^{(1)} \cdot G^{(2)} \cdot G^{(3)} = A_k^3 \cdot T_1 T_2 T_3 \cdot e^{\alpha_k (V_1+V_2+V_3)} \tag{2.13}$$

where T_1, T_2, and T_3 are the transparencies of the three GEMs.
The gain results a function of the sum of the all voltage supplies, V_{tot}. In addition, it depends on the gas mixture characteristics, on the transparencies (i.e. the electric field configuration) and on the sum of voltage supplies, V_{tot}.
With a detector based on triple-GEM it is possible to study the phenomena that occur during the ionization process inside the gaseous region crossed by a charged particle. The events readout can be achieved by using the signal induced by the electrons on appropriate electrodes, or collecting the light emitted by the de-excitation of the gas molecules through high granularity optical sensors as Charge Coupled Devices (CCD) or Active Pixel Sensors based on Complementary Metal-Oxide-Semiconductor (CMOS).

2.3 Optical readout principle

During the avalanche process the scattering of electrons with the gas atoms or molecules can produce photons trough electro-luminescence phenomenon [11].
The CYGNO innovative approach to TPC involves the detection of the photons produced by the de-excitation of gas molecules during the processes of electron multiplication. The light yield and spectrum strongly depends on the gas and operating conditions. Thanks to the recent developments in both the performance of Micro Pattern Gas Detectors and the evolution of the CMOS technology, this approach can achieve very high granularity and tracking precision. The optical readout principle is based on innovative technological and operational choices:

- the use of triple-GEM system which provides very high and uniform gas gains combined with high granularity at the amplification stage;
- the use of scientific CMOS-based cameras (sCMOS) positioned behind the amplification plane for the detection of the scintillation light produced together with the electron avalanche in the GEMs. These devices offer a high granularity 2D readout along with very high sensitivity in the visible range ($>$ 90% of quantum efficiency at 600 nm);
- the combination of the sCMOS 2D X-Y track projection with the signal from a Photomultiplier (PMT) for the detection of the time profile of charge arrival. Thanks to this, the relative track extension along the drift direction (ΔZ) and the inclination with respect to the amplification plane can be inferred, and 3D reconstruction can be achieved with O(100) μm precision;
- the use of an He:CF_4 60:40 gas mixture at 1 atm, with spectral emission at 600∼nm (as the figure 2.9 shows) nicely matching the sCMOS camera sensitivity.

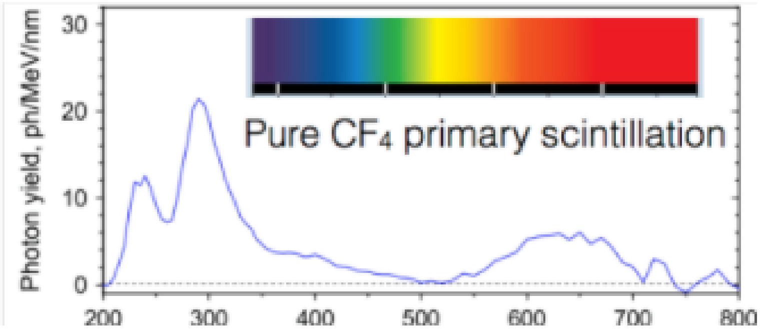

Figure 2.9. Emission spectrum of CF_4

Given the kinematic of the WIMP-nucleus elastic process, a direct DM detection experiment achieves its best sensitivity for WIMP masses equal to the target mass nuclei. Thanks to its low density and atomic number, the use of helium can hence extend CYGNO sensitivity to low O(GeV) WIMP masses for spin independent coupling and allow to reach atmospheric pressure operation while maintaining good tracking. The CF_4 is added for its well-known scintillation properties in the visible region, where sCMOS cameras have the maximum sensitivity. In addition, CF_4 large Fluorine content provides a spin-odd target for simultaneous sensitivity to spin dependent WIMP-proton interactions;

- the atmospheric pressure and room temperature operation: while increasing the available target mass compared to current gaseous directional DM approaches, it also minimises the infrastructures needed and overall experiment dimensions, costs, and material budget;
- the decoupling of the readout sensor from the gas target volume, not possible with charged-based readouts. This avoids the readout outgassing into the target, modifying the gas properties or producing recoiling radon progeny in or near the active detector volume, relatively relaxing the radiopurity requirements.

2.4 The CMOS-sensor and PMTs

The CMOS-sensor used in the CYGNO experiment is the ORCA-Fusion Digital CMOS camera. The ORCA-Fusion provides an excellent low-light application performance of any sCMOS camera available. To achieve this, it is important focusing on two parameters that are especially relevant to camera performance in photon-starved conditions: read noise and read noise uniformity. The importance of low read noise for low light signal detectability is well known and relatively easy to appreciate: the lower the noise floor the lower the threshold for detecting signal. The importance of read noise uniformity is a less discussed parameter that has only come to the forefront with the advent of sCMOS cameras, due to the nature of CMOS structure [7].
The basic principle of operation of the camera is the following: incoming photons are converted to photo-electrons via the photoelectric effect in the sensitive layer of

the silicon substrate.

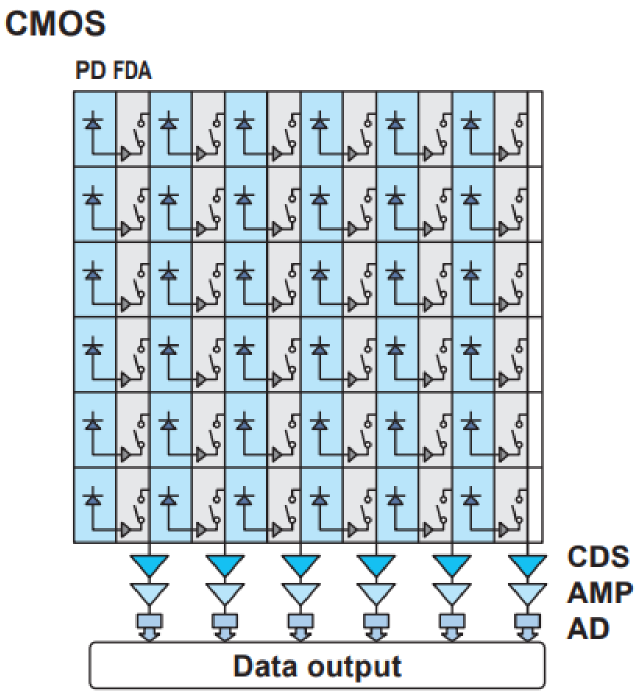

Figure 2.10. Pixel structure and readout pathway in CMOS sensor. CMOS is an array of photodiodes that are able to detect light by converting photons into electrons. Its structure detects photons as photoelectrons and this charge is immediately converted to a voltage within each pixel. That voltage is then converted to digital units. Because CMOS pixels are read out in parallel, the overall speed of each electrical component can be slow, keeping the read noise low, but the total read out speed, and therefore, frame rates are still fast.

This electron charge is next converted to a voltage, then amplified again and converted to a digital signal through an analog to digital converter (ADC). An image is formed when the charge from each pixel is converted to a digital signal; this process is called readout. The charge is converted into a voltage within each pixel and then additional amplification and analog to digital conversion is achieved in column ADCs. The pixel structure and read out pathway are shown in figure 2.10. Pixel signal to noise ration (SNR) is a standard metric used to express camera sensitivity.

sCMOS-sensor exhibits very low noise (less than 2 photons/pixel), has low power consumption, and offers larger field of view compared to Charged Coupled Devices combined with smaller pixels ($6.5 \times 6.5\ \mu m^2$). The picture 2.11 shows the ORCA-Fusion camera features.

An example of images HAmamatsu sCMOS camera is shown in figures 2.12a and 2.12b.
The optical readout principle of CYGNO experiment foresees the combined use of sCMOS-sensor and the PMTs.

A PMT is a vacuum electron tube which generates and amplifies electric current

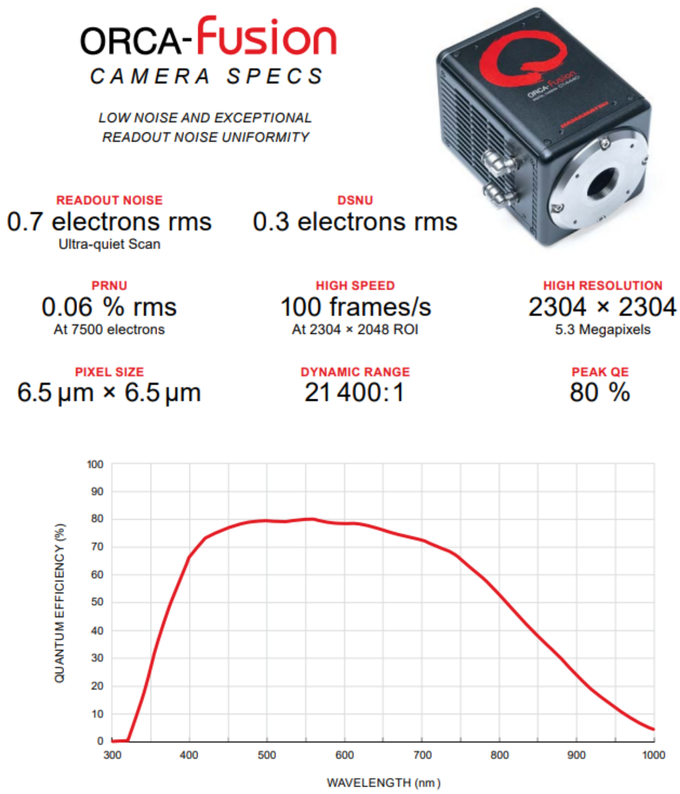

Figure 2.11. The ORCA-Fusion CMOS camera features. The readout noise is equal to 0.7 $e^{-}rms$, the resolution is high and equal to 2304 $pixels \times$ 2304 $pixels$, the size of each pixel is $6.5\mu m \times 6.5\mu m$, and the Quantum Efficiency is of 80%. The spectral response is obtained by studying the Quantum Efficiency as function of wavelength which shows a maximum in the range between 500 nm and 600 nm.

in response to sollecitations of a luminous nature. It has two functions: sensitivity to electromagnetic radiation in the visible region (phototube) and behavior of a multistage amplifier (electronic multiplier). In other words, vacuum photomultipliers are photon detectors that translate the optical signal into electrical signal. The signal is generated when a photon hits the photo-cathode and, by photoelectric effect, it is absorbed generating a photo-electron. The latter is accelerated by an electric field and creates a cascade of photo-electrons in the various subsequent electrodes (dynodes) up to the anode, where the signal is picked up. The figure 2.13 shows the principle of operation of a PMT.
PMTs used in this experiment are PMTs Hamamatsu R7378A which have a maximum supply voltage equal to 1200 V and a gain of 2.0×10^{6}.
The general characteristics of a PMT are as follows:

- Quantum efficiency (QE): it is the probability that a photon generates a photo-electron by the photoelectric effect. In percentage it is defined as

$$QE = \frac{number\ of\ e^{-}\ produced\ by\ photocathode}{number\ of\ photons\ collected\ on\ the\ photocathode} \tag{2.14}$$

  The quantum efficiency depends on the wavelength λ of the photons produced.

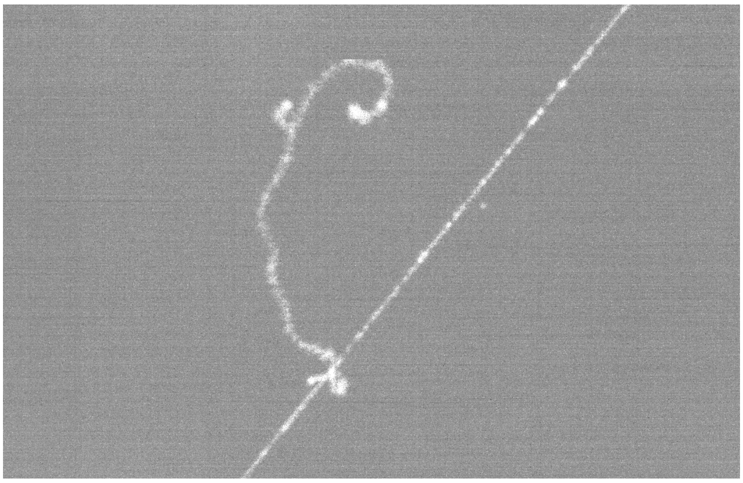

(a)

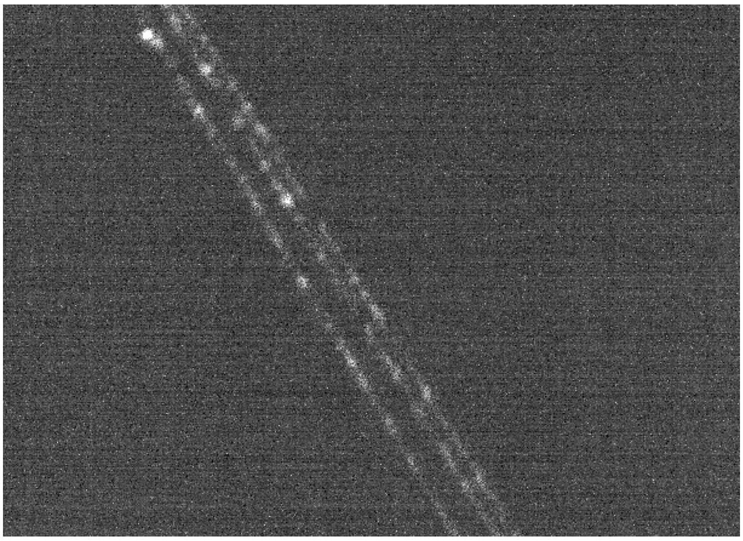

(b)

Figure 2.12. Examples of tracks produced by particles interacting with an He:CF_4 60:40 gas mixture at 1 atm and captured by the sCMOS camera. It is possible to note by looking the image 2.12b the capability of the camera to separate two or more tracks well.

The PMT is therefore chosen by adapting it to the spectrum of light produced in the detector (400 ÷ 500 nm) and the typical values of the QE. They are included between 20% and 30%.

- Geometrical Efficiency (GE): fraction of produced photons that are collected.
- Gain: it is defined as the number of final electrons with respect to the initial photo-electrons. A chain of resistances creates an accelerating field between the various dynodes present. For each of these last ones, the multiplication factor (which indicates how many times the signal is multiplied) varies from 3 ÷ 5. Calling n_k the number of incident electrons and the gain of the first dynode g_1, the number of secondary photo-electrons resulting is equal to $n_k g_1$.

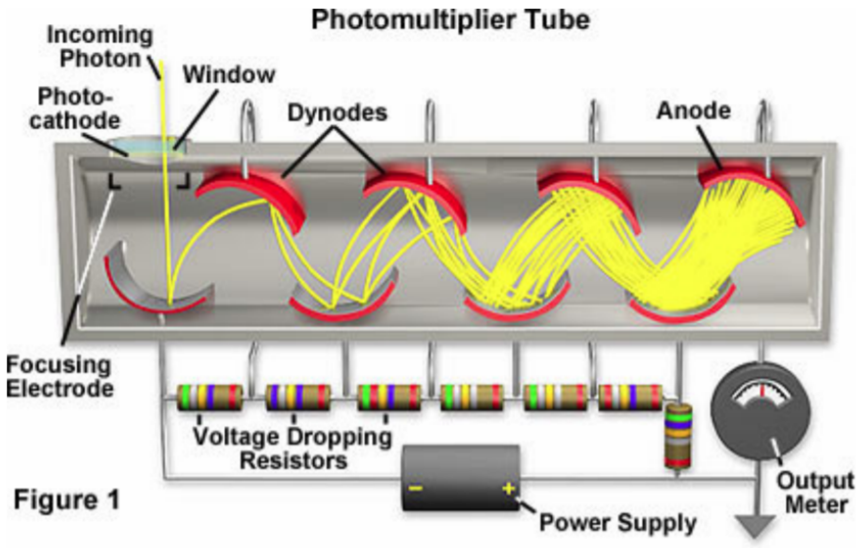

Figure 2.13. Working principle of a photomultiplier (PMT). An incoming photon reaches the photocathode and beacause of the photoelectric effect a photo-electron is emitted. The photo-electron reaches the first dynode and the electrons produced during the multiplication process reach the anode, where they are converted in an output signal.

If the second dynode has a gain of g_2, the secondary photo-electrons will be $n_k g_1 g_2$ and so on. If the number of dynodes is N, the number of photo-electrons collected is:

$$n_a = n_k \prod_{i=1}^{N} g_i \tag{2.15}$$

The total gain depends on the number of dynodes present.

- Noise: the noise inside a PMT can be of two types:
  - the noise given by secondary effects which are not produced by the photo-electrons (background), but for example by electrons produced by the thermionic effect. This generates a dark current due to the thermal noise of the cathode and dynodes or eddy currents, described by the Richardson equation:

    $$J = AT^2 \exp\left(-\frac{W_{th}}{KT}\right) \tag{2.16}$$

    A is a constant which depends on the type of material and T is the temperature; K is the Boltzmann constant and W_{th} is the work of extraction of the material composing the photocathode and dynodes of the PMT;
  - the noise given by the presence of residual materials inside the tube, which can be ionized from the photo-electrons generating delayed currents that produce the after-pulse phenomenon.
- Reply in time: how quickly the cascade (and therefore the signal) is generated following the arrival of a photon;

- Linearity: the light emitted is proportional to deposited energy.

PMTs and CMOS camera are complementary. In the case of PMTs the light signal is fast, so the PMTs are able to measure the time in which the light was emitted; while in the case of CMOS camera, the light is added on a very long gate (10 - 100 ms) compared to 10 - 100 ns of the PMTs signal.

Chapter 3

The LIME prototype

3.1 Detector description

The LIME (Long Imaging ModulE) detector is the largest TPC prototype of CYGNO experiment and it concludes the phase-0 of this project. It was conceived to have the same drift length and the same readout scheme of the final demonstrator of CYGNO.
LIME was built at Frascati National Laboratory and it is going to be installed underground at Gran Sasso National Laboratory in early 2022. The detector has a 50 liter sensitive volume and it has a 50 cm long drift path. LIME is divided in several components:

- **Gas Vessel**: a gas mixture is enclosed in a vessel made by plexiglass. In the centre of the upper face there is a window of ETFE (ethylene-tetrafluoroethylene) 125 μm thick, 5 cm wide and as long as the field cage (50 cm). This window was designed to be able to perform test with low energy radioactive sources. ETFE has higher tensile strength and higher heat resistance than PTFE (polytetrafluoethylene) used in the past. The pictures 3.1 and 3.2 show LIME detector.

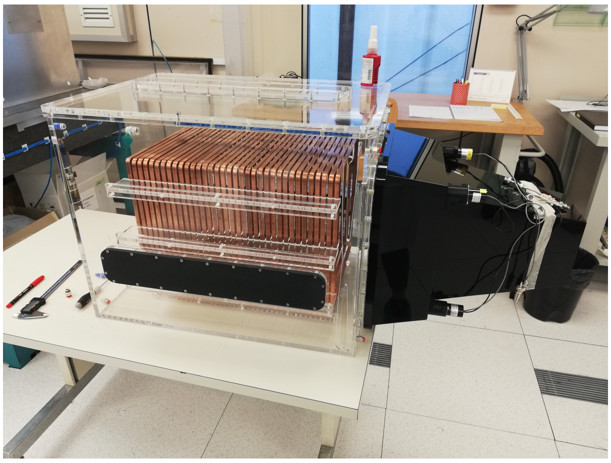

Figure 3.1. Picture of LIME detector being prepared for data taking.

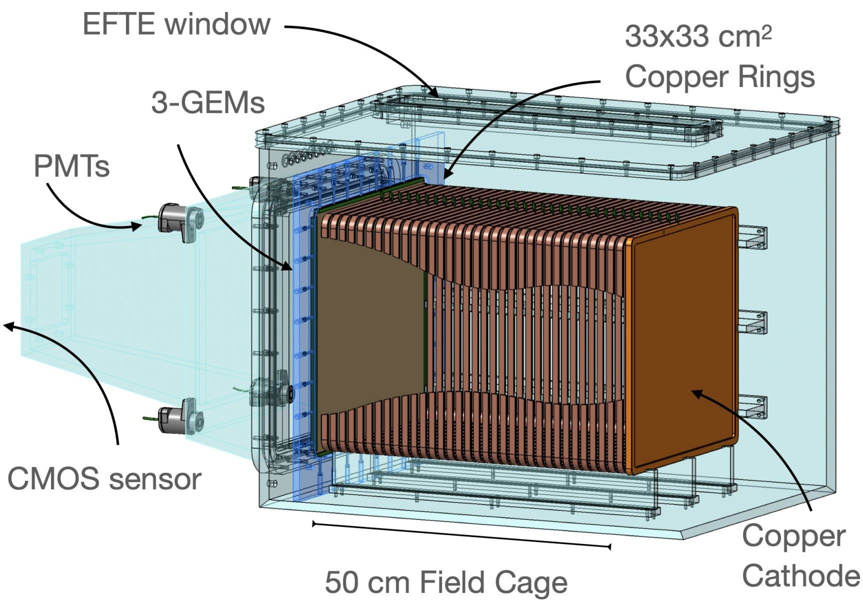

Figure 3.2. Drawing of LIME detector. It is possible to see the different components of LIME, such as the field cage composed by copper rings (the brown region), and the box of plexiglass which surrounds the field cage. The triple-GEM system and the cathode also are drawn in the figure and they are placed at the ends of the field cage.

- **Triple-GEM**: the anode is composed by a thin triple-GEM system with a $33 \times 33 \ \ cm^2$ surface. Each GEM is at the nominal working point equal to 440 V so as to generate a higher electric field. Due to the presence of such an electric field electronic avalanche processes occur in GEM channels and secondary electrons together with photons are produced. The triple-GEM system is shown in the pictures 3.3a and 3.3b.

- **Cathode**: on the opposite side of triple-GEM system there is the cathode which collects the positive ions produced by interaction between gas molecules and particles travelling through the detector. The cathode is at voltage equal to about 50 kV. In addition, it is composed by about 3 mm thick copper as shown in the figure 3.4.

- **Field cage**: in the gas vessel a field cage is placed. It is composed by copper rings (figure 3.5) conveniently roundly shaped to avoid discharges at a 16 mm pitch. 100∼MOhm resistors are used to connect the rings in series and to connect to the cathode the ring closest to it. In this way, a voltage difference applied between the cathode and the ring closest to the GEMs produces a uniform electric field (drift field in the following) in the sensitive volume.

- **sCMOS-sensor**: an ORCA-Fusion Digital CMOS camera allows us to capture images of light spots and particles tracks produced in sensitive volume of LIME. The camera has 2304 $\ \ pixels \times 2304 \ \ pixels$ high resolution, pixels size of $6.5\mu m \times 6.5\mu m$, a readout noise of 0.7 electrons rms and a Quantum Efficiency maximum of 80 % that correspond to a wavelength of 600 nm. Taking into

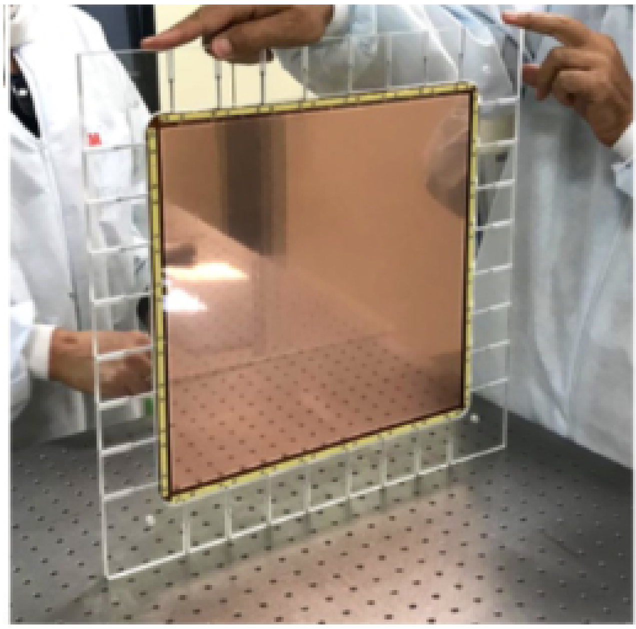

(a) Picture of GEM system before proceeding with its installation in LIME.

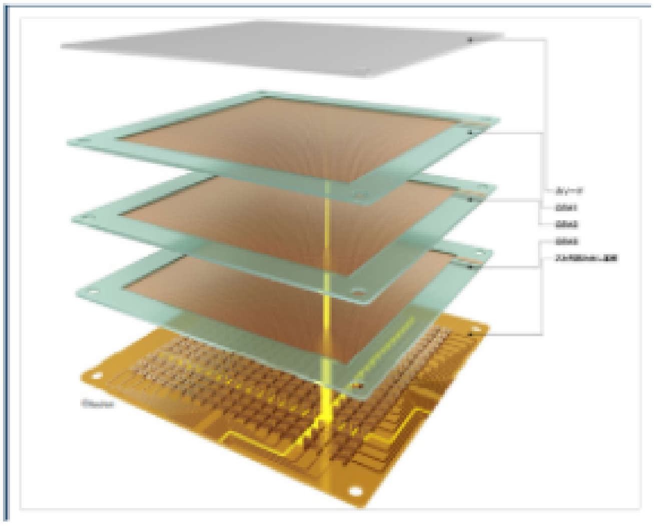

(b) Drawing of broken GEMs. The three GEMs are well separated and it is possible to see how each GEM is composed.

Figure 3.3. Picture and drawing of tryple-GEM system.

account the quantum efficiency, the response of the sensor is about 2 counts per photon. The counts are the contents of each pixel readout.

- **Camera lens**: sCMOS camera has a Schneider-Kreuznach lens with 0.95

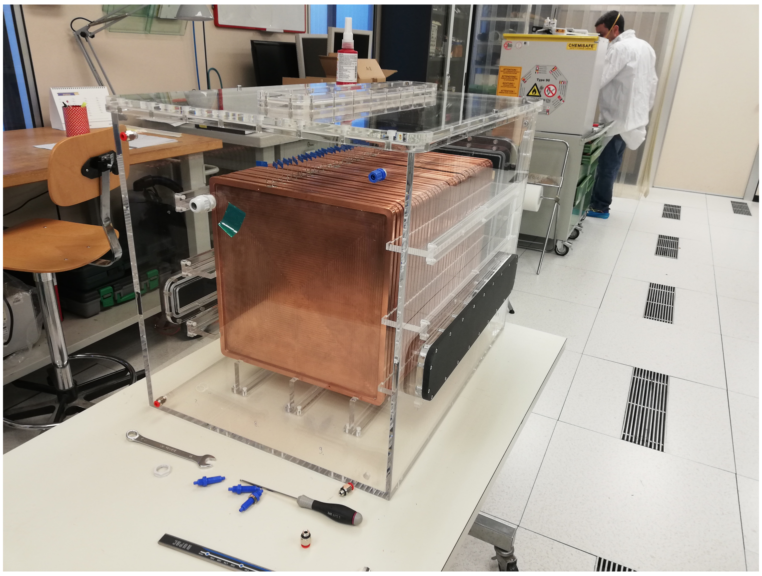

Figure 3.4. The cathode of LIME detector

Figure 3.5. Copper rings of the field cage of LIME viewed from the above.

optical aperture and 25.6 mm focal length.

- **4 PMTs**: the light produced by electronic avalanche processes is collected by 4 PMTs symmetrically placed around the sCMOS-sensor at a distance of about 15 cm from it and 25 cm apart from the GEM surface. We used PMTs Hamamatsu R7378A with a maximum supply voltage of 1200 V and a gain of 2.0×10^6. The combined use of CMOS and PMT technology allow 3D reconstruction of events as it is explained in the article on the Combined readout of a triple-GEM detector [13]. The pictures 3.6a and 3.6b show CMOS sensor and PMT used.

(a) ORCA-Fusion Digital CMOS sensor.

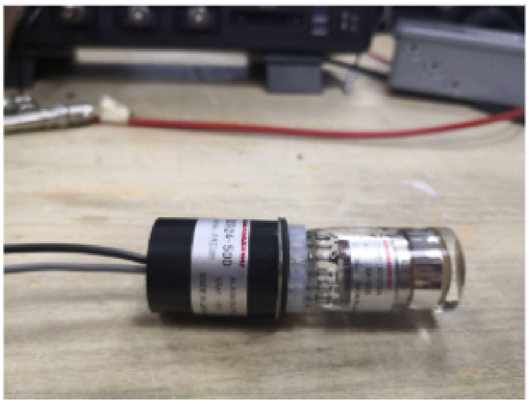

(b) Hamamatsu R7378A PMTs.

Figure 3.6. Pictures of CMOS sensor and one of four PMTs used for combined readout.

- **Faraday cage**: LIME detector in enclosed in a Faraday cage of 2 mm thick aluminium that isolates the detector from electromagnetic interference (figure 3.7).

- **Gas mixture**: the vessel of LIME is filled by a gas mixture of He/CF_4 (60/40) kept at atmospheric pressure. This mixture is expected to have an emission spectrum with a main contribution around 600 nm characteristic of the CF_4, as reported in the picture 2.9. At the peak of this spectrum the camera provides a Quantum Efficiency of 80 %.

3.2 Test setup at Frascati Laboratories

Before to proceeding with the installation of LIME at LNGS we have studied the detector performances by means of a ^{55}Fe source. The source emits photons with an energy of about 5.9 keV. When a photon emitted by the source enters the gas vessel, it interacts with the gas atoms or molecules by photoelectric effect and produces an

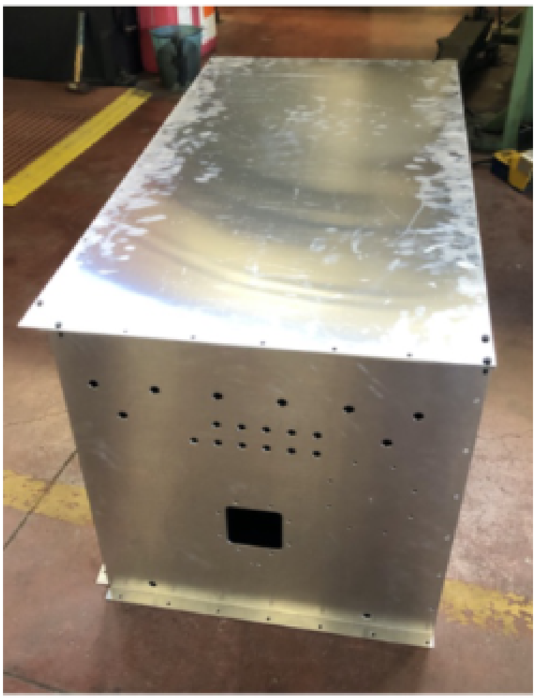

Figure 3.7. Faraday cage of aluminium

electron at 5.9 keV. The electron produced randomly walks through the gas volume for 500 ± 200 μm, and it densely ionizes producing 150 primary electrons.
A charge cloud reaches the GEMs and finally produces a light spot like those ones shown in the figure 3.8.

Figure 3.8. Light spots produced by the electronic cloud when it reaches the GEMs. The electronic cloud is composed by primary electrons produced by the interaction between the photo-electron and the gas atoms or molecules.

The different tests on LIME done at LNF were performed with the experimental setup shown by the picture 3.9. The field cage, PMTs and triple-GEM system are powered by means cables that are red, blue and black in the figure 3.9.

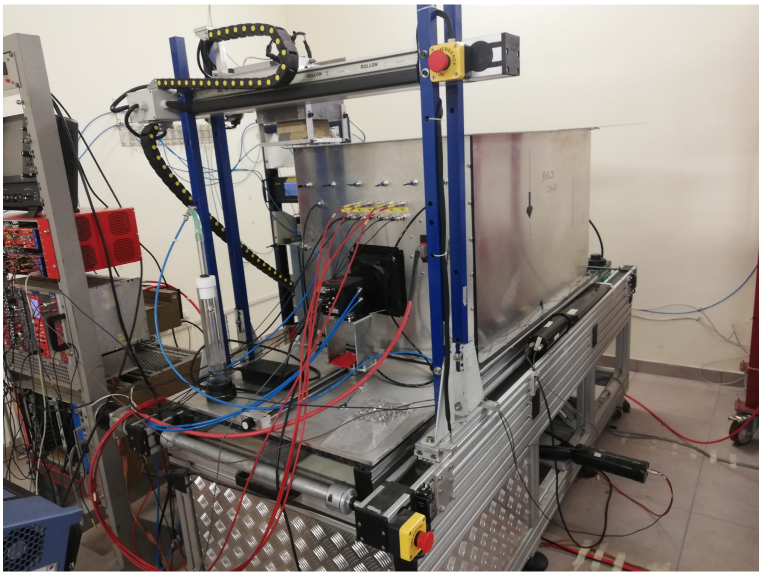

Figure 3.9. Experimental setup of LIME. Red, black and blues cables carry voltage to the different components of detector.

The goal of tests performed with LIME was to study the features of the detector and its capability to detect the particles crossing its gas sensitive volume. For this purpose we have taken experimental measurements with source placed at different positions from GEM surface and at each position we changed the High Voltage (HV) applied to GEM1 (defined as GEM1 HV in the following). The source was placed along z-axis, so as the position of the source varies, the z coordinate changes. The light spots are brighter closer to the sensor because the brightness depends on the distance between the source of light and the sensor: the shorter the distance the greater the brightness.

3.2.1 Camera setup

In order to take the images of light spots we used the global reset function of CMOS sensor. This function synchronizes the camera to the external equipment. We created the external trigger with a pulses train. Global reset function enables to reset the electric charge of all pixels at the same time. Then all pixels can start exposure at the same time. The exposure of all pixels begins on the edge timing of the input trigger signal into the camera. The picture 3.10 shows the different features of global reset function of the sensor.

The light produced during the multiplication processes in the triple-GEM system was recorded with an exposure time of 10 ms for both pedestal runs and data runs.

3.2.2 Data Acquisition

We have taken data with an exposure of two different types:

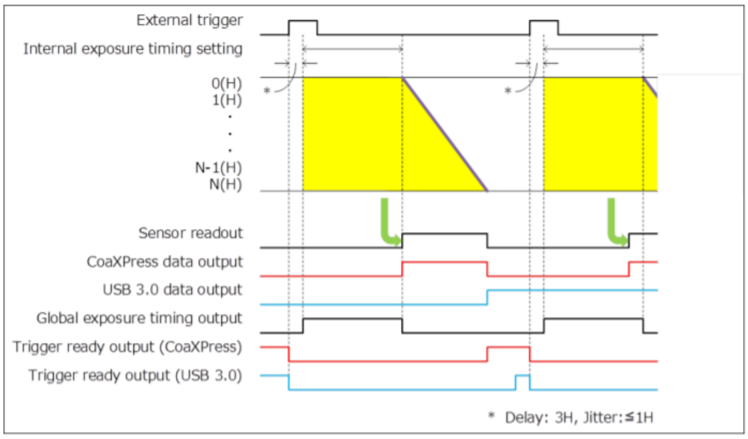

Figure 3.10. Global Reset External Trigger mode configuration. The yellow region corresponds to the exposure of pixels of camera. All pixels start exposure at the same time as shown by the yellow rectangle. The yellow triangle corresponds to the sensor readout.

- pedestal: we acquired 200 images with sensor in total dark, GEM off and without the source. These experimental measurements are useful for studying and subtracting the electronic noise of the sensor.
- with source: runs of 200 images each were acquired with a ^{55}Fe source placed in the Faraday cage and GEM on.

We changed the position of source with a carriage in a range between 5 cm and 45 cm with a step of 5 cm. For each value of z we took a run of pedestal with GEM off and 7 runs with different values of voltage applied to GEM1. In this thesis we report only the results of some: one scan in z and one in GEM1 HV.
In addition to the electronic background a natural radioactive background due to cosmic rays and natural radioactivity is present in the data collected, as shown by the image 3.11a.

3.2.3 Data Analysis

The analysis algorithm is based on three steps:

- **Pedestal subtraction**: A run of pedestal is acquired at each position of source. For each pixel, the pedestal is evaluated as the average number of counts recorded in this run and it is subtracted to the counts collected in all recorded images.
- **Clustering**: A simple Nearest Neighbor-Cluster (NNC) clustering algorithm was used. A lower resolution version of each image was created with macro-pixels made by matrices of 4×4 pixels. The average count over the 16 pixels, after subtracting their pedestal values, is assigned to each macro-pixel. A cluster is reconstructed by at least two neighbouring macro-pixels having more than 2 counts each. The Figures 3.11a and 3.11b are images of clusters obtained by using this algorithm.

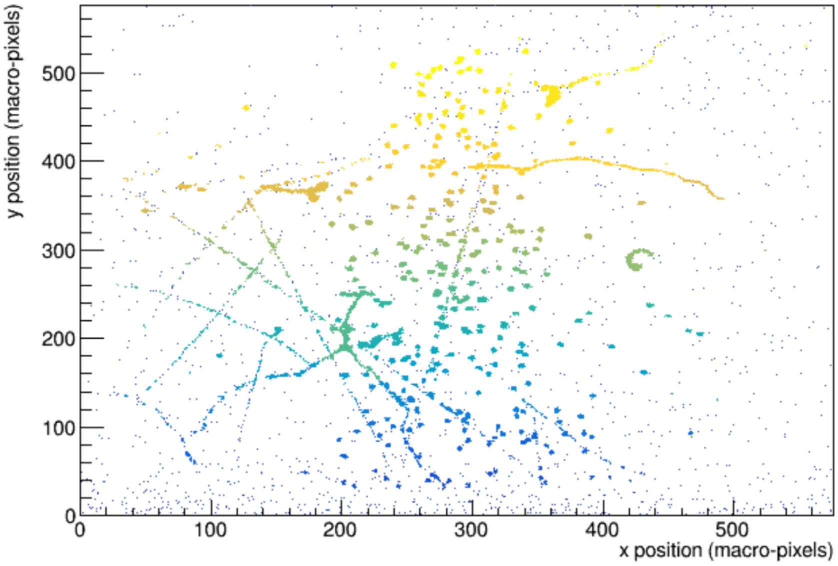

(a) The picture shows an image of light spots reconstructed by the algorithm of the analysis. As we can see some of reconstructed light spots correspond to interactions of photons emitted by the radioactive source. The other spots are due to the presence of natural radioactivity. It is possible to see the track of muons that crossed the detector. This image represents a lower resolution version of the images taken by the sensor. For this reason the plot is composed by macro-pixels made by matrices of 4×4.

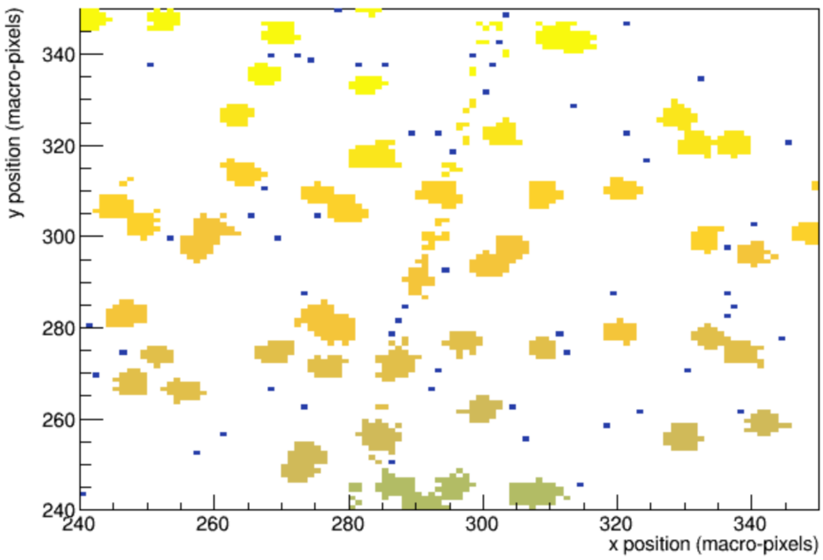

(b) A zoomed image of reconstructed spots collected by the CMOS sensor. In order to obtain this image we have enlarged the central region of the Figure 3.11a.

Figure 3.11. Pictures of reconstructed light spots of run with source placed at z = 20 cm.

- **Images Analysis**: An algorithm was used to analyze all 200 images and to study all the features of the clusters counted with the NNC clustering algorithm.

In order to maximize the ratio signal/background we concentrated our analysis on the region where the number of clusters was greater and the light spots were due to interactions of photons emitted by the radioactive source with gas atoms. For this reason, we selected clusters with $y > 288\ macro-pixels$ and $250\ macro-pixels < x < 325\ macro-pixels$.
The features of the clusters that we studied are:

- **Clusters light (l_{clu}):** for each run l_{clu} was estimated by adding the counts of each pixel within the cluster placed in each image of run.
- **Size (s_{clu}):** the size of each clusters was estimated by counting the number of pixels that compose the cluster itself.
- **Position:** the position of each cluster is defined by the x_{clu} and y_{clu} coordinates of cluster itself.
- **Radius (ρ):** the radius was estimated as the distance between the position of each cluster and the centre of the image:

$$\rho = \sqrt{(x_{clu} - x_{clu0})^2 + (y_{clu} - y_{clu0})^2} \tag{3.1}$$

  where x_{clu0} and y_{clu0} are the coordinates of the centre of the image.
- **Slimness (S):** the slimness is defines as

$$S = \frac{\Delta X}{\Delta Y} \tag{3.2}$$

  where ΔX corresponds to the minor axis and ΔY to the major axis of a cluster.

Our goal was to find a correlation between radius and l_{clu}. In order to do this, we imposed several requirements in the selection of clusters. We selected only clusters with:

- S in a range between 0.6 and 1 in order to pick out clusters with an almost circular shape;
- size in a range around the peak of its distribution;
- $l_{clu} > 1000$.

3.2.4 Voltage Settings

The different values of voltage applied on GEM1 performing the scan in GEM1 HV are 440 V, 431 V, 420 V, 406 V, 386 V, 350 V, and 320 V. These values are estimated by the eq. 3.6 in the section 3.4. The voltages of GEM2 and GEM3 were fixed at 440 V. In addition, the values of drift and transfer fields are $E_{drift} = 0.9kV/cm$ and $E_t = 2.5kV/cm$.

3.3 Study of the response uniformity

The goal of this measurement was to study the response uniformity of the detector as function of the position of the event and the light collected.

3.3.1 Optical effects

The first step of the analysis was to study l_{clu} as a function of radius. The plot 3.12 shows the dependence of l_{clu} on the radius. As we can see in Fig. 3.12 l_{clu} depends on the distance of the spot from the centre of the image. This trend of l_{clu} is expected to be mainly due to the so-called vignetting effect.

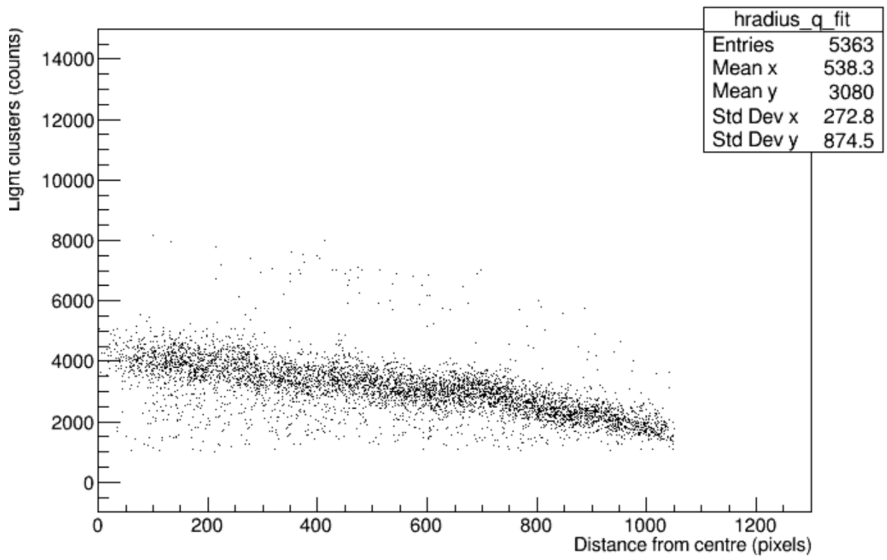

Figure 3.12. Clusters light vs distance from centre with source placed at 20 cm. The value of l_{clu} decreases as the distance from the centre of the image decreases.

Vignetting effect refers to the radial fall-off of brightness away from the centre of an image. It is mainly caused by foreshortening of light rays at oblique angles to the optical axis and by obstruction of light by the stop or lens rim [11]. The vignetting effect is typical of all optical systems. In the case of our lens, we expect to lose up to 60% - 70% of light on the edges. This effect is undesirable because we are interested to study the light of spots produced by source in any point of detector. For this reason the light collected has to be independent of the distance from the centre of the image.
We analyzed run with the source at 20 cm from the GEM surface. In order to correct the dependence of l_{clu} on radius, we fitted l_{clu} trend with a quadratic function:

$$l_{clu} = a\rho^2 + b\rho + c \tag{3.3}$$

where $a,\ b,\ and\ c$ are the parameters of the function. We imposed the initial parameters of the fit in such a way as to best approximate the data. The plot 3.13 shows the fitted trend of l_{clu} as function of radius.

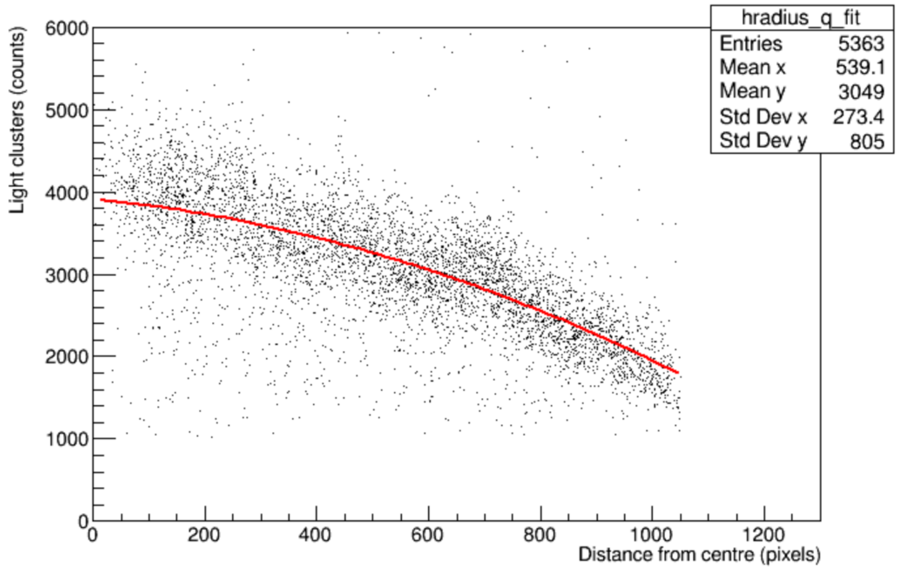

Figure 3.13. Light of clusters vs radius fitted by a quadratic function. The parameters of fit function are $a = -0.0013 \pm 0.0001$, $b = -0.64 \pm 0.15$ and $c = 3906 \pm 37$.

Then, we obtained the corrected l_{clu} trend as shown by the plot 3.14 normalizing l_{clu} by the fit function obtained by averaging the fits of all z. This normalization will be explained in the section 3.3.2. As the Figure 3.14 shows, l_{clu} corrected with the fit has a constant trend. After correcting the behavior of l_{clu} as function of radius we filled a histogram with all values of l_{clu} counted for every cluster and we obtained the distribution shown by the Figure 3.15.

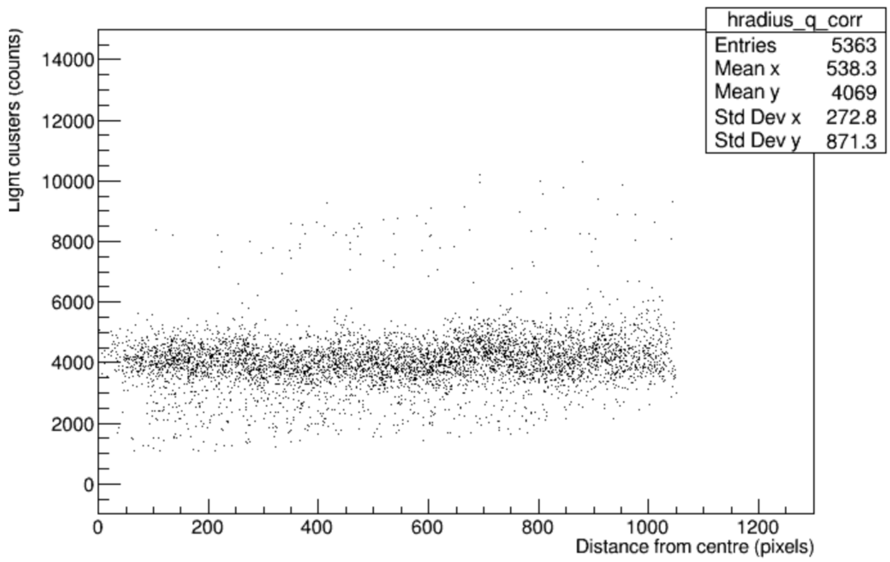

Figure 3.14. Behavior of l_{clu} as function of distance from centre after normalizing by the average fit function (eq. 3.3). The trend of l_{clu} is constant as we move towards the edges of image.

The plot 3.15 shows that three peaks are present in the corrected l_{clu} distribution. The first peak corresponds to a single light spot, the second one corresponds to two spots not well separated, and the third peak to more spots not separated. We fitted the distribution of l_{clu} obtaining parameters that allow us to estimate the quantities of interest. The fit is composed by the sum of 5 functions: 4 gaussians and an exponential. As the Figure 3.15 shows each peak of distribution is approximated by the corresponding function to check its shape. The first peak is approximated by the green function and it corresponds to single spots. The second one is represented by the purple function and it corresponds to double spots. A single spot corresponds to a single photon interacting with a gas atom, while a double spot is composed by 2 clusters generating by the interactions of 2 different photons that the algorithm of analysis could not separate. The light distribution shows also the contribution of natural radioactive background drawing by the yellow function and that one of electronic noise which is approximated by the black function. By studying the distribution of l_{clu} we could estimate the number of photons per eV (n_γ/eV) and the energy resolution (R_{en}) shown in section 3.3.3.

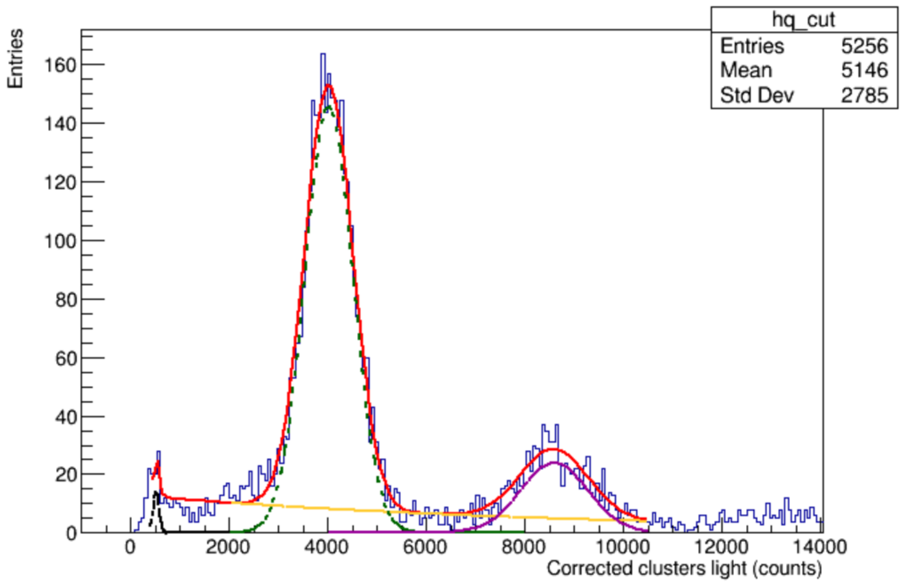

Figure 3.15. Light distribution of clusters: the green function corresponds to single spots, the purple one to double spots. The yellow and black functions approximates the environmental, detector radioactivity and electronic noise.

3.3.2 Drift Field effects

After studying light distribution and the behavior of light as function of radius at a certain z position of the radioactive source, we analyzed using the same method runs corresponding to the other z of source. First of all we fitted the light trend as function of distance from centre at every position of source to study the vignetting effect.

The next step was to estimate the average value of each function and to divide the three parameters of function by the respective average value. The average value

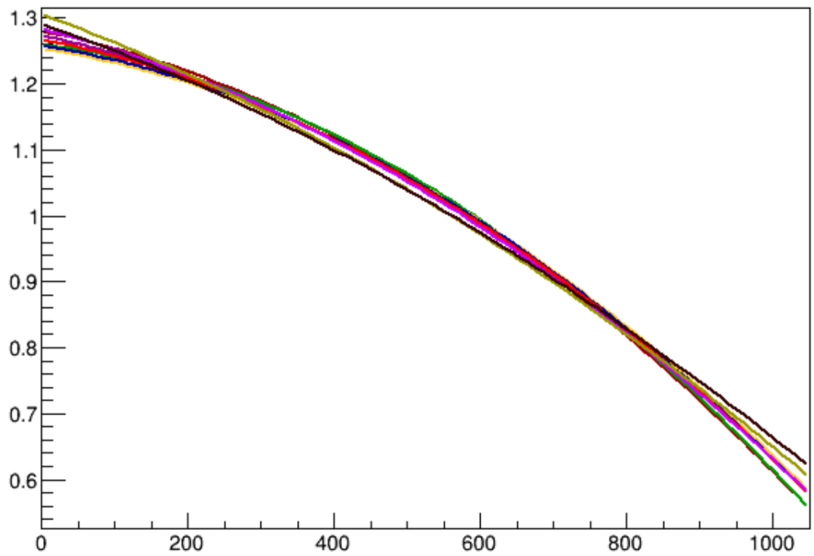

Figure 3.16. Fit functions obtained for different positions of source. The red function corresponds to function estimated by averaging all fits.

was estimated by using the following formula:

$$f_m = \frac{1}{\Delta r} \int_{r_1}^{r_2} f(x)dx \tag{3.4}$$

where $\Delta r = r_2 - r_1$ is the range of integration. In our case $r_1 = 0$ and $r_2 = 1050$, so $\Delta r = 1050$. Then, we estimated the average function of those ones obtained by using the new parameters. The Figure 3.16 shows the different fits obtained after normalizing each fit function for the estimated average value. As we can see in Fig. 3.16, he absolute value depends upon the z coordinate, while the shape of fit functions does not depend upon the position of source. The red function in the plot 3.16 is the average function we obtained.
The dependence of light on the radius is not due to the position of source. Therefore, the knowledge of the z of the event is not crucial to correct for the response dependence on distance from the centre that is likely only due to the optical effect.

3.3.3 Dependence on z

The next step was to estimate l_{clu} and R_{en} for each position of source. The values of l_{clu} were estimated by the mean parameter of fit of the peaks corresponding to the light spots. The relative uncertainties were obtained by the errors of the fit. Table 4.1 contains the values of l_{clu} of first peak for each z.

We plotted the values of l_{clu} as function of z and we obtained the Figure 3.17.

The energy resolutions were estimated by using the following relation

$$R_{en} = \frac{\sigma}{\mu} \tag{3.5}$$

where σ and μ are the standard deviation and the mean of distribution fit, respectively. The uncertainties associated with R_{en} were estimated by the propagation of

Position of source (cm)	l_{clu} *of first peak (counts)*
5	3044 ± 10
10	3519 ± 11
15	3846 ± 10
20	4029 ± 10
25	4063 ± 12
30	3899 ± 13
35	3740 ± 14
40	3606 ± 13
45	3550 ± 22

Table 3.1. Values of l_{clu} at different positions of source from GEM surface.

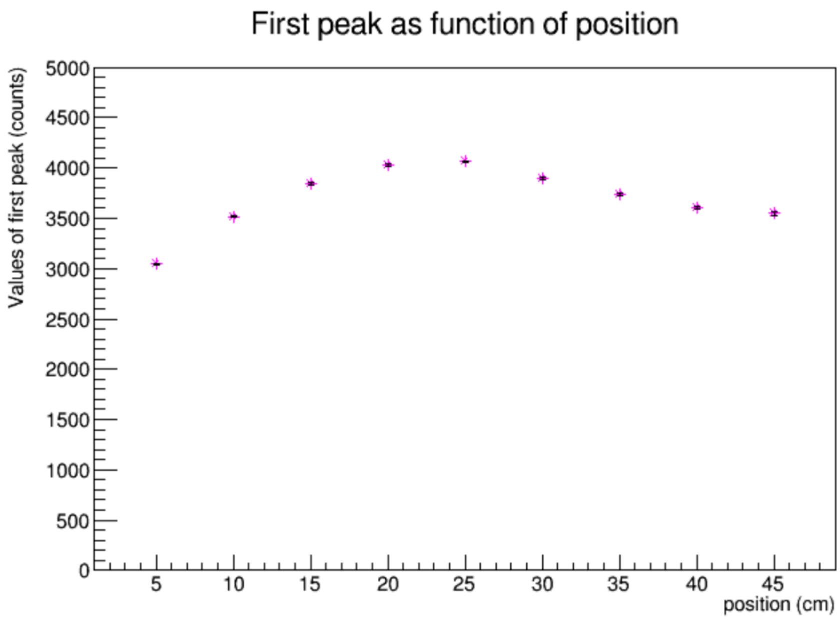

Figure 3.17. Value of first peak as function of z position. Each point is shown with its own uncertainty obtained by the error of the fit.

uncertainties. The values of R_{en} estimated by analyzing the first peak of distribution of l_{clu} and the second one are contained in table 3.2.

The values of energy resolution of first and second peak were plotted as function of z and we obtained the Figures 3.18 and 3.19.

The plots 3.17, 3.18 and 3.19 show these quantities as function of z coordinate. Their trend is due to the overlap of two effects:

- GEM gain dependence on the charge density in the multiplication channels. Since this dependence modifies the amplification field, shielding it, the effective gain for signals, produced far from the GEMs, is greater since the charge density is moderated by the diffusion effects in the gas. This explains the increase of the response as z increases;

Position of source (cm)	***Energy Resolution of first peak***	***Energy Resolution of second peak***
5	0.15 ± 0.02	0.10 ± 0.08
10	0.14 ± 0.02	0.10 ± 0.07
15	0.12 ± 0.02	0.09 ± 0.07
20	0.12 ± 0.02	0.08 ± 0.06
25	0.13 ± 0.02	0.08 ± 0.07
30	0.14 ± 0.02	0.08 ± 0.08
35	0.13 ± 0.03	0.10 ± 0.09
40	0.15 ± 0.02	0.10 ± 0.10
45	0.14 ± 0.12	0.13 ± 0.06

Table 3.2. Values of R_{en} of first and second peak at different positions of source from GEM surface with their relative uncertainties.

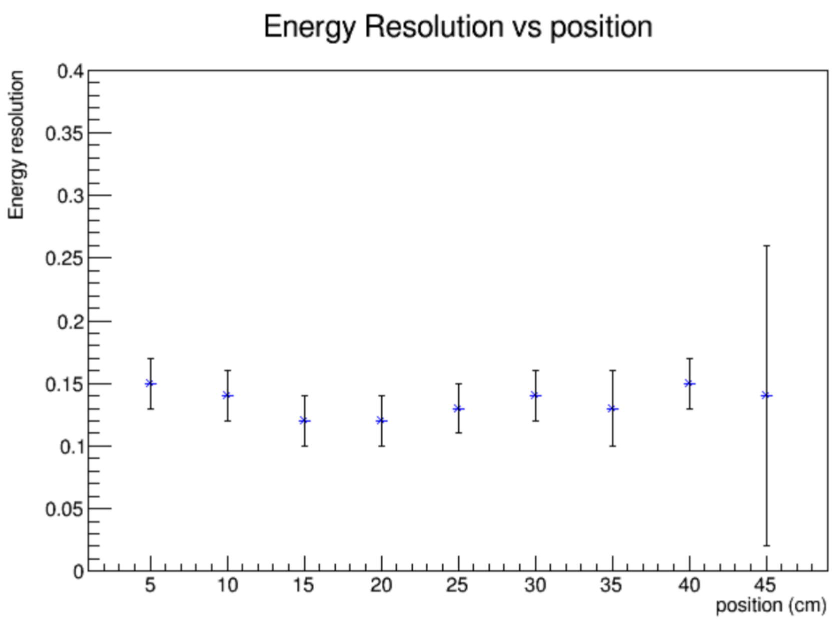

Figure 3.18. Energy resolution of first peak as function of z position

- charge absorption due to recombination, for instance during the drift, causes the response to drop to high z.

Since we will not know the z coordinate in the real experiment we created a cumulative light spectrum of all runs analyzed which is shown in Figure 3.20.The energy resolution of first peak of this cumulative spectrum was 0.17 ± 0.01, while the energy resolution of second peak was 0.12 ± 0.05.

3.4 Response linearity

In order to study the response linearity of LIME detector we did measurements in a given position of source by changing the voltage applied to the first GEM. Our goal was to study the response of LIME to low energy releases. Since we did not have sources emitting particles with an energy smaller than 5.9 keV we simulated the release of this energy by decreasing the voltage applied to GEM1, so by decreasing

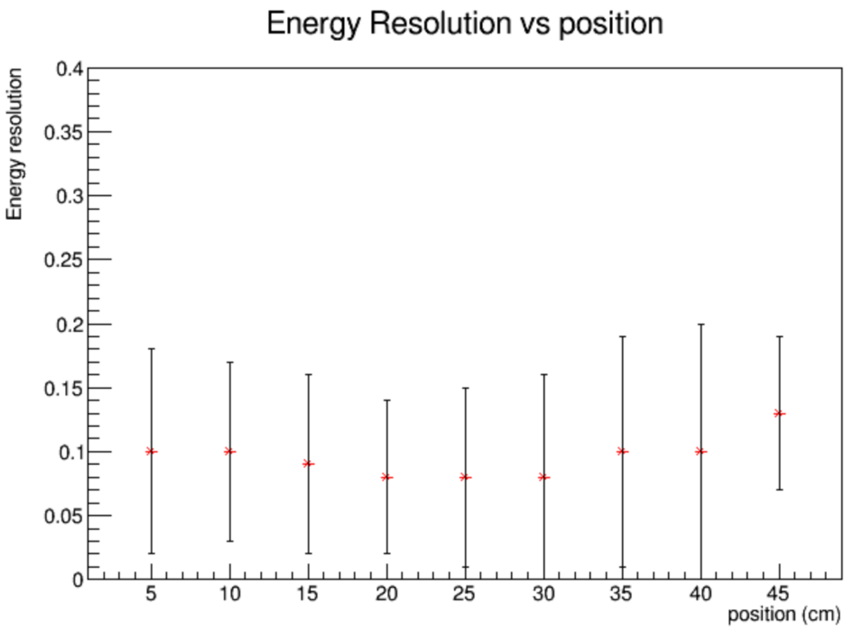

Figure 3.19. Energy resolution of second peak as function of z position

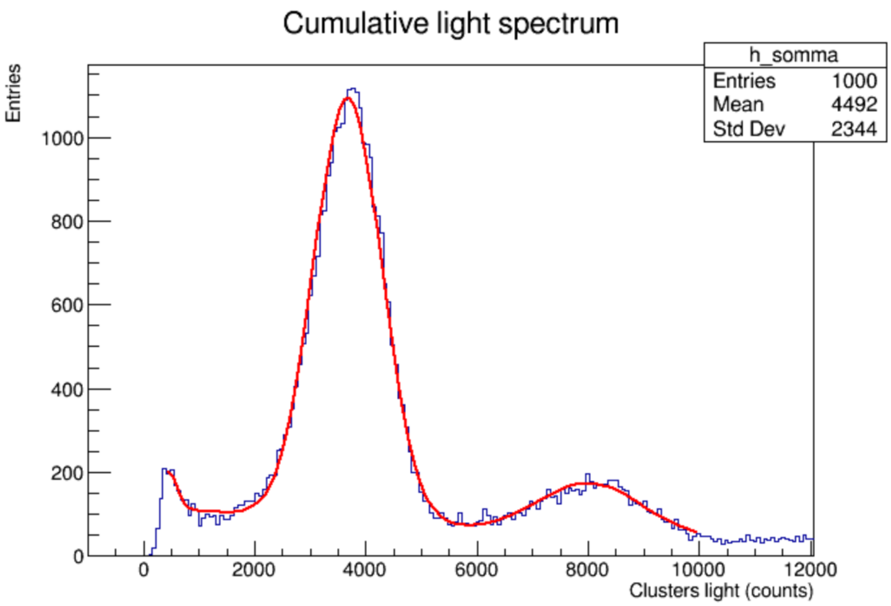

Figure 3.20. Cumulative light distribution of clusters obtained by overlapping distributions of all z positions.

the gain of one GEM. We have placed the ^{55}Fe source at 20 cm from the GEM surface and we the different voltages applied were 440 V, 431 V, 406 V, 386 V, 350 V and 320 V. Since we measured that the gain follows the formula:

$$G = 0.0303 \cdot e^{0.0189 \cdot V} \tag{3.6}$$

we used it to estimate the values of voltages to applied on the GEM1 simulating 5.1, 4.1, 3.2, 2.2, 1.1 and 0.6 keV.
In the formula, G is the gain of the GEM and V is the difference between the voltage that corresponds to G=1 (440 V) and the voltages lesser. We associated with each gain an energy that is a fraction of 6 keV (photon energy).
The table 3.3 shows the values of GEM1 HV and the equivalent particle energies.

GEM1 HV (V)	Equivalent Particle Energy (keV)
440	6.0
431	5.1
420	4.1
406	3.2
386	2.2
350	1.1
320	0.6

Table 3.3. Values of GEM1 HV and the equivalent particle energies.

3.4.1 GEM1 HV scans

The algorithms used to do the analysis were the same used to study the response uniformity. After using the clustering software to construct the number of clusters in each image we did several cuts to select clusters with certain features. The requirements adopted on S and s_{clu} were equal to those ones used in previous analysis. Then, we studied the trend of l_{clu} as function of radius and we corrected it by fitting the light trend. Finally, we plotted the distribution of l_{clu} of each run. The Figure 3.21 shows the l_{clu} distribution of run at 406 V.

By looking the plot 3.21 it is possible to note the contribution of natural radioactive background (green function) and two peaks corresponding to single and double spots (yellow and purple functions).
Even at equivalent energies of about 1.1 keV and 0.6 keV the peak of the signal is evident as the Fig. 3.22 and 3.23 show and gives an average value, shown in Fig. 3.27, in good agreement with expectations. This result is a first evidence of the possibility of this technique of operating even below the keV energy release threshold.

Thanks to the fit of the distribution we estimated l_{clu}, s_{clu}, and R_{en} and we studied these quantities as function of GEM1 HV. The values of l_{clu} of first peak are in table 4.3 with their relative uncertainties.

The plot 3.24 is filled by the values of l_{clu} at different GEM1 HV.

The Figure 3.24 shows l_{clu} increases as GEM1 voltage increases.
Then, we filled a histogram with values of s_{clu} and we fitted the distribution with a gaussian function that approximated the peak of distribution. s_{clu} was obtained by considering the mean parameter of fit, while the relative uncertainty was the error obtained by the fit. The results of this study are reported in table 4.4.

The results reported in table 4.4 were studied as function of GEM1 HV. The plot 3.25 shows the behavior of size with the variation of GEM1 HV.

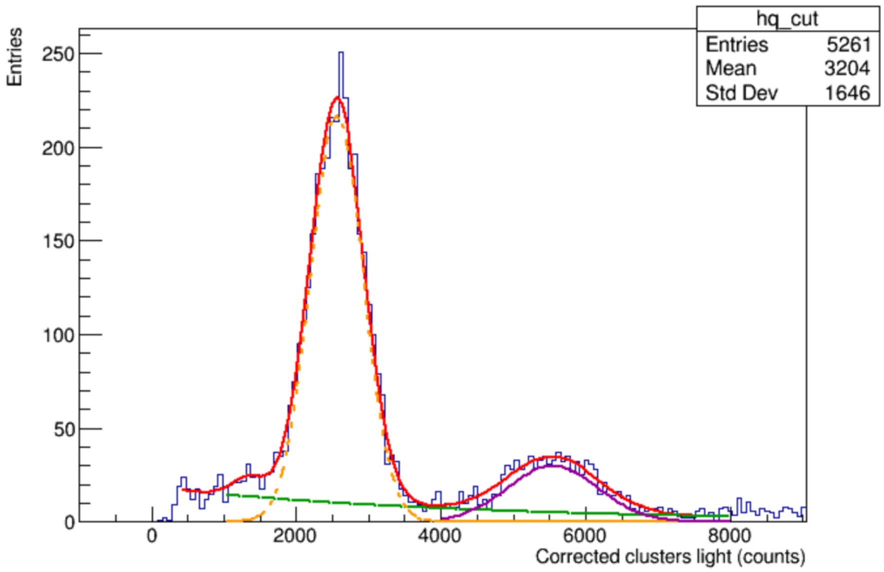

Figure 3.21. l_{clu} distribution of run at 406V. The yellow function approximates the peak corresponding to single spots, the purple function peak corresponding to double spots and the green function the environment and detector radioactivity.

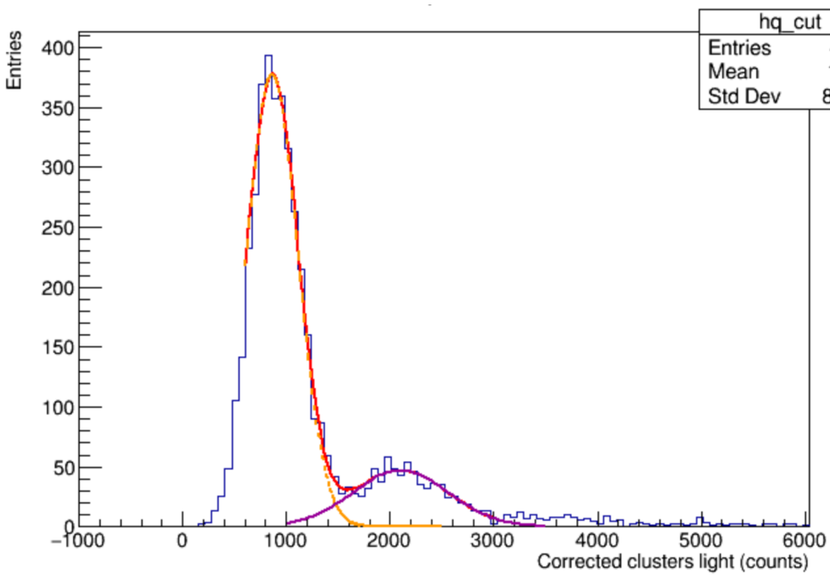

Figure 3.22. l_{clu} distribution of run at 350V. The yellow function approximates the peak corresponding to single spots; the violet function approximates the second peak that corresponds to double spots.

s_{clu} is proportional to the value of GEM1 HV as we expected. At lower voltages of GEM1 light spots are less bright and for this reason the clusters consist of fewer pixels.

Finally, we estimated R_{en} by considering mean and standard deviation of fit of light distribution. The energy resolution was estimated for runs at different values of

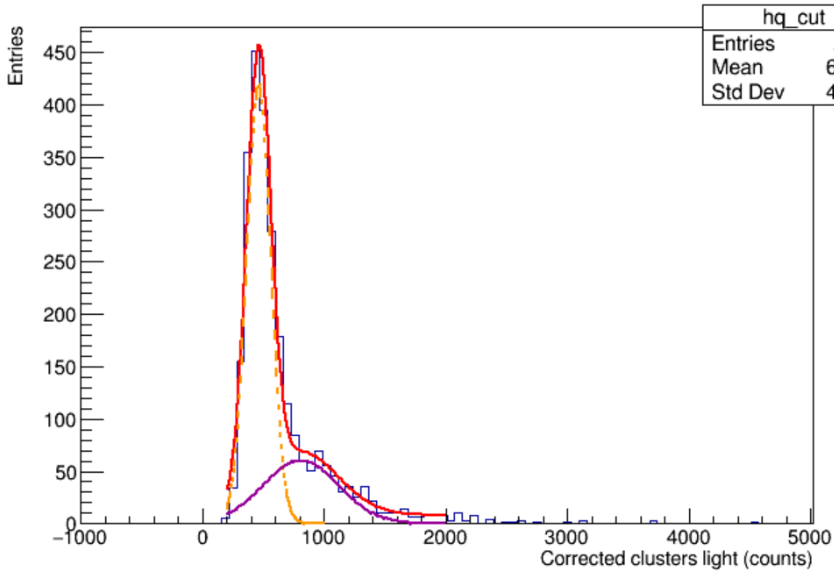

Figure 3.23. l_{clu} distribution of run at 320V. The yellow function approximates the peak corresponding to single spots; while the violet function approximates the second peak that corresponds to double spots.

GEM1 HV (V)	***Equivalent Particle Energy (keV)***	l_{clu} ***of first peak (counts)***
440	***6.0***	4029 ± 10
431	***5.1***	3579 ± 10
420	***4.1***	3079 ± 9
406	***3.2***	2567 ± 8
386	***2.2***	1903 ± 6
350	***1.1***	870 ± 1
320	***0.6***	465 ± 3

Table 3.4. Values of l_{clu} at different GEM1 HV with relative uncertainties.

GEM1 HV (V)	***Equivalent Particle Energy (keV)***	s_{clu} ***(pixels)***
440	***6.0***	355.5 ± 0.6
431	***5.1***	333.7 ± 0.5
420	***4.1***	314.5 ± 0.5
406	***3.2***	286.5 ± 0.5
386	***2.2***	247.1 ± 0.4
350	***1.1***	167.8 ± 0.4
320	***0.6***	98.9 ± 0.4

Table 3.5. Values of s_{clu} at different GEM1 HV with relative uncertainties.

GEM1. The results of analysis are in table 4.5.

The plot 3.26 shows the trend of energy resolution as GEM1 HV decreases.

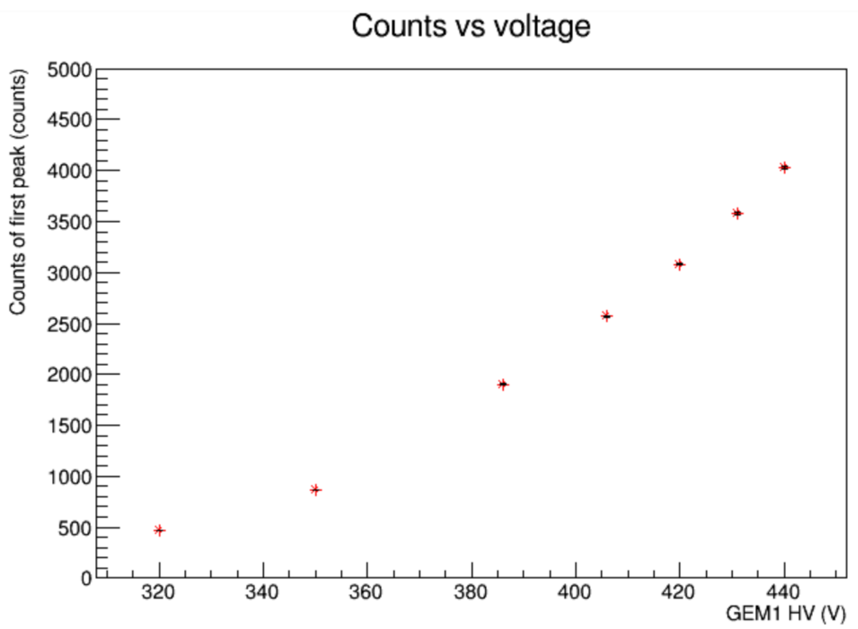

Figure 3.24. Behavior of l_{clu} of first peak as function of voltage applied to the first GEM. The light of clusters increases as the GEM1 HV increases.

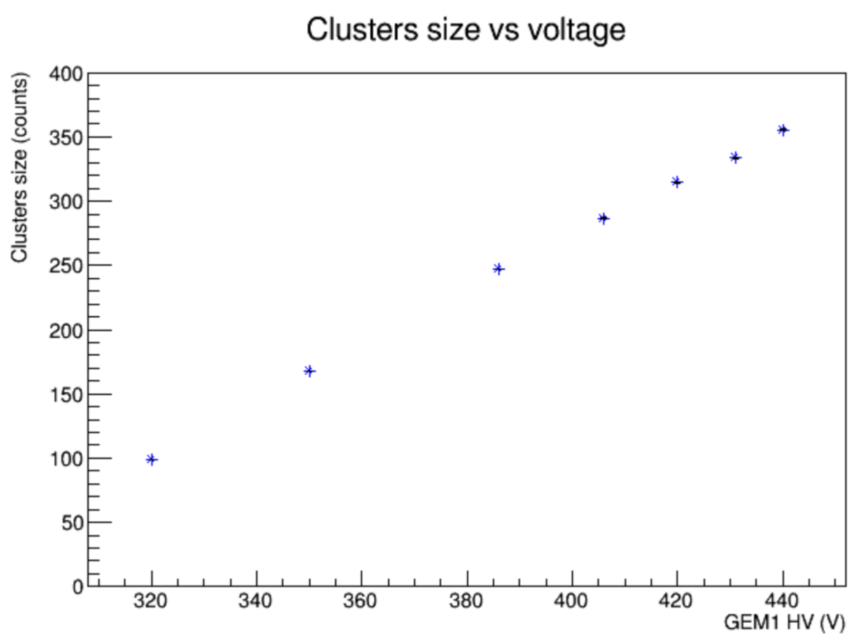

Figure 3.25. Clusters size as function of voltage applied to GEM1

As we can note by looking the Figure 3.26 R_{en} is higher at low voltages and decreases as the voltage increases. This effect can be explained with a lower relative fluctuation of the GEM gain for higher voltage.
By replacing voltage values with respective energy values in the plot 3.24 it was possible to check the response linearity of detector. l_{clu} decreases as the energy of

GEM1 HV (V)	*Equivalent Particle Energy (keV)*	*Energy Resolution*
440	*6.0*	0.12 ± 0.02
431	*5.1*	0.12 ± 0.02
420	*4.1*	0.13 ± 0.02
406	*3.2*	0.14 ± 0.02
386	*2.2*	0.16 ± 0.02
350	*1.1*	0.28 ± 0.01
320	*0.6*	0.22 ± 0.04

Table 3.6. Values of R_{en} at different GEM1 HV with relative uncertainties. R_{en} are obtained by the ratio between μ and σ of fit.

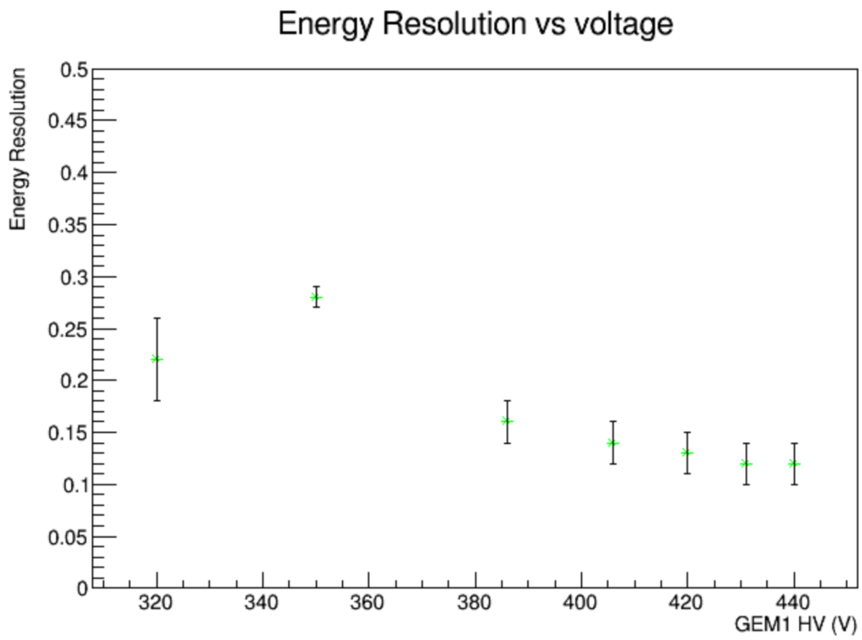

Figure 3.26. Energy resolution as function of voltage applied to the first GEM.

particles decreases. The plot 3.27 shows this trend.

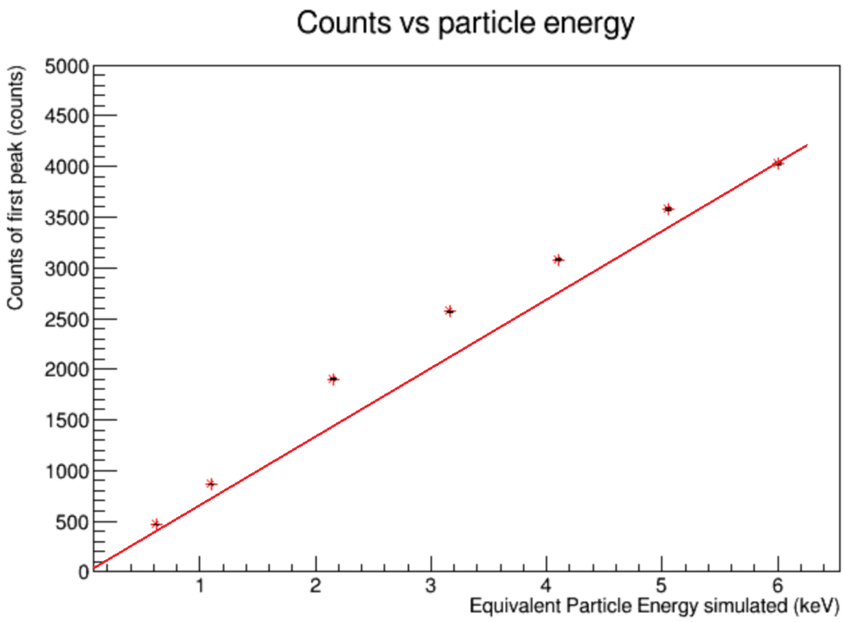

Figure 3.27. Behavior of l_{clu} of first peak as function of particles energy. The response increases with the equivalent energy of the particle, even if the behavior is not linear. This is well reproduced by simulation (see next chapter Fig. 4.4) indicating that the GEM1 HV settings were not properly chosen.

Chapter 4

Data comparison with simulation

4.1 Simulation method description

The simulation is the study of behavior of a detector through its reproduction in a context that we can control. It is important because the simulation allows us to make predictions about detector response as signal and background features change. In order to understand the results of an experiment we need to compare data events with simulated events.
The simulations of experiments are made by using the so-called Monte Carlo (MC) method. MC simulation is a model used to predict the probability of different outcomes when the intervention of random variables is present. In other words, MC method uses random numbers to simulate behavior of elementary units so as to predict overall behavior of the system.
The most common application of Monte Carlo method in particle physics consists in simulating the passage of radiation through the matter and predicting the response of detector. The simulation develops by propagating particles in the medium of interest. First of all, we consider only one primary particle with a given energy and direction. Then, we observe its interactions with several elements that compose the system. Each interaction causes a variation of particle energy and direction and secondary particles can be emitted. The tracking procedure continues iteratively until primary and secondary particles are absorbed by the medium or emerge from the simulated volume. Since MC method is a statistic approach we need to repeat this procedure many times. In order to estimate the average evolution of system we have to track many identical primary particles.
In the last years, one of Monte Carlo programs mostly used in physics is Geant4. It is a toolkit containing all the useful and necessary tools to simulate a true detector. In defining and implementing the software components, all aspects of the simulation process have been included: the geometry of the system, the materials involved, the fundamental particles of interest, the generation of primary particles of events, the tracking of particles through materials and external electromagnetic fields, the physics processes governing particle interactions, the response of sensitive detector components and many others. Users just have to choose the tools that are useful for

their goal and use them.
The goal of our study was to simulate features of LIME detector and compare data with MC to demonstrate the goodness of simulation. The simulation was composed by several steps:

- **reconstruction of 5.9 keV photon interaction**:
  Geant4 was used to reproduce processes that happen in the detector. In other words, with this simulation program for each event the emission of a photon with an energy of 6 keV was simulated. Its interactions with gas molecules or atoms and the propagation of secondary particles were also simulated. The outcomes of this part were the positions of hits in the gas, such as the interaction points of particles, and the relative energy deposits.

- **imaging by sensor reconstruction**:
  After reconstructing the emission of photons and their propagation and interaction in the gas volume, we had to reconstruct the image containing the particle tracks. For this purpose we needed to simulate:

  - transport of electrons up to the GEM: absorption and diffusion
  - electrons multiplication in the GEM
  - saturation on the last GEM
  - light collection

  We used a light yield of 0.07 photons/electrons [12] and an active area of $35\ cm \times 35\ cm$. The value of light yield was measured from the GEMs that we had used and it represents the emission of the light from the GEM. The sensor features used for the simulation were a camera aperture of 0.95, a granularity of $2304\ pixels \times 2304\ pixels$, a sensor size of 14.976 mm and a sensor calibration of 1 photon every 2 sensor counts. The parameters of the gas mixture relevant to the electrons transport in the field cage (discussed in sections 2.1.1 and 2.2) were calculated by means of a simulation program called Garfield. Because electrons diffuse along their drift in the field cage, when they arrive on the GEM they trigger avalanche multiplications of an area larger than the ionization region. The photons emitted by gas electro-luminescence in the avalanches create the light-spots on the sensor. The geometrical efficiency of light collection was estimated as:

  $$\Omega = \frac{1}{(4(d+1)\cdot a)^2} \tag{4.1}$$

  where d is

  $$d = \frac{image\ size}{sensor\ size} = \frac{350\ mm}{14.976\ mm} = 23.37 \tag{4.2}$$

  and a is the camera aperture.

- **Event simulation**:
  In order to obtain MC data with features similar to those ones of experimental data we simulated the z scan and GEM1 HV scan. So, for z scan we used a range between 10 cm and 45 cm, while for GEM1 HV scan we impose the following values of voltage on GEM1: 350 V, 386 V, 406 V, 420 V, 431 V, 440 V. GEM2 and GEM3 were fixed with a voltage equal to 440 V.

4.2 Study of response uniformity

As it is reported in the previous section, the goal of the comparison between experimental and MC data is to demonstrate the goodness of simulation. For this purpose, the first step of our study was to compare experimental and MC results in response uniformity.
We took MC events obtained by simulating different positions of source and the corresponding data events. Both data events and MC events were reconstructed and analyzed with the same code. The code used is that one described in section 3.2.3 in chapter 3.

4.2.1 Dependence on z

Regarding the data, we selected clusters with an almost circular shape in the range between 0.6 and 1, as discussed in chapter 3, and with a size higher than 100 pixels. After doing these requirements we proceeded with the analysis of light distribution. By studying the light distribution of clusters at each position of source for both data and MC, we obtained the results reported in the following table 4.1. The table 4.1 contains the results of data events and MC events. The position of source is that one measured on the carriage.

Position of source (cm)	l_{clu} ***of data (counts)***	l_{clu} ***of MC (counts)***
10	3519 ± 11	2926 ± 28
15	3846 ± 10	3432 ± 33
20	4029 ± 10	3741 ± 42
25	4063 ± 12	4059 ± 52
30	3899 ± 13	4291 ± 53
35	3740 ± 14	4374 ± 52
40	3606 ± 13	4405 ± 66
45	3550 ± 22	4391 ± 65

Table 4.1. Values of clusters light at different positions of source from GEM surface. The position is measured on the carriage where the source is. These values of light are estimated by studying experimental events and MC events.

Then, we plotted the results reported in table 4.1 as functions of source position. The plot 4.1 shows the trend of clusters light as the source changes its position.

As the plot 4.1 shows at small distances from GEMs data and MC have a similar trend until z is equal to 25 cm. At values of z higher than 25 cm the trend of data is below that one of MC and the difference between the results is higher. Probably, this behavior is due to an underestimation of the absorption parameter.

An other quantity studied was the energy resolution. This quantity was estimated as the formula 3.5 shows for both data and MC. In order to get the energy resolution at each position of source we took the mean and the standard deviation resulting from gaussian fit of clusters light distribution. The relative uncertainty was estimated

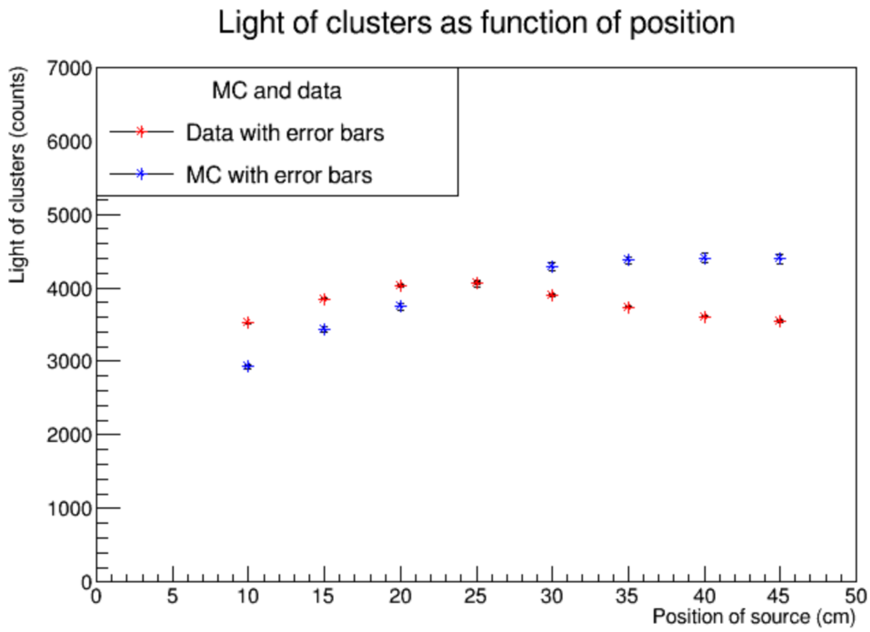

Figure 4.1. Behavior of data events and MC events. At low z the data follow a similar trend. At z higher than $z = 25cm$ data are below MC.

by the propagation of uncertainties. The values of energy resolution obtained from data events and MC events are reported in the table 4.2.

Position of source (cm)	R_{en} ***of data***	R_{en} ***of MC***
10	0.14 ± 0.02	0.09 ± 0.07
15	0.12 ± 0.02	0.09 ± 0.08
20	0.12 ± 0.02	0.11 ± 0.08
25	0.13 ± 0.02	0.12 ± 0.08
30	0.14 ± 0.02	0.12 ± 0.08
35	0.13 ± 0.03	0.12 ± 0.07
40	0.15 ± 0.02	0.15 ± 0.08
45	0.14 ± 0.12	0.14 ± 0.08

Table 4.2. Values of energy resolution at different positions of source from GEM surface and relative uncertainty. These values are estimated by studying data and MC.

In order to compare the values of energy resolution obtained by studying both data and MC we put them in a plot and studied their trend. The Figure 4.2 shows the behavior of data events and MC events energy resolution as the position of source changes.

The trends of energy resolution can be considered constant. At higher distances from GEM the energy resolution increases both in the case of data and in that one of MC. As we can see in table 4.2 and by looking the plot 4.2 data have a higher energy resolution than MC.

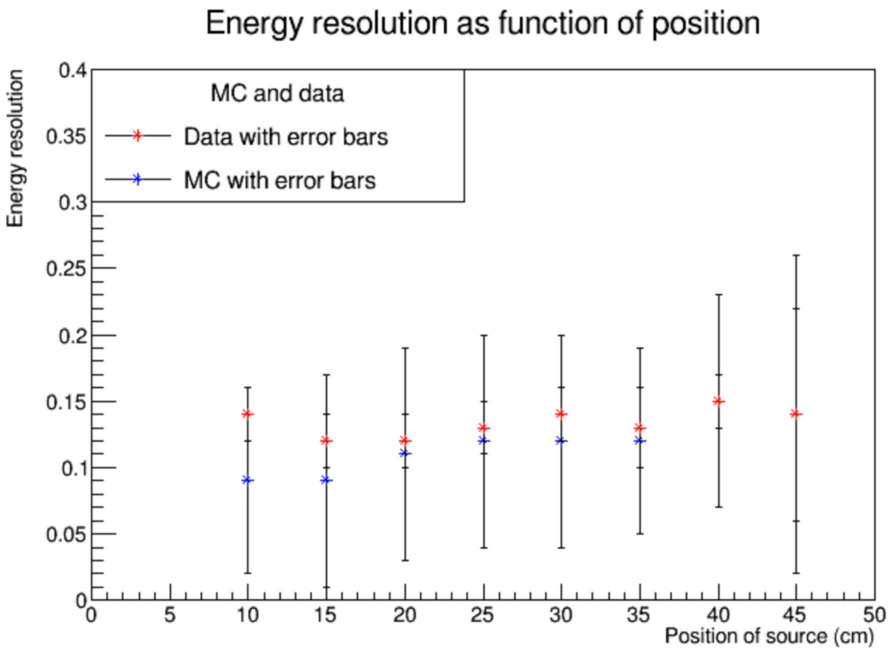

Figure 4.2. The plot shows the comparison between experimental and MC energy resolutions. They appears similar and their behavior is almost constant.

4.3 Response linearity

The next step of our study was to analyze data events and MC events with different values of HV applied to GEM1. The goal of this study was to compare the results by demonstrating that they are valid and to check the response linearity of LIME detector. The cross-check between data events and simulated events allowed us to accept results obtained by the study of detector response at different HV of GEM1. The different values of voltage correspond to different low energies of particles travelling through the sensitive volume.
In order to compare the results obtained by studying data and those ones resulting by analyzing MC, for runs corresponding to data we selected clusters placed in a square with sides equal to 500 pixels. An other requirement adopted for the analysis of data was to select only clusters with an almost circular shape and with a size higher than 100 pixels. Before proceeding with the study of clusters light to estimate the value of light for each run, we corrected the vignetting effect by dividing the light by the fit function obtained in the previous studies (3.16).

4.3.1 GEM1 HV scan

We studied the distribution of clusters light of each run that corresponds to a given value of voltage and we estimated the light of clusters at different voltages of GEM1. We did analysis for both data and MC. Table 4.3 contains values obtained by our analysis with their relative uncertainties resulting from the parameters of the distribution fit. The voltage corresponding to an energy of 0.62 keV was not simulated.

GEM1 HV (V)	l_{clu} ***of data (counts)***	l_{clu} ***of MC (counts)***
440	4029 ± 10	3741 ± 42
431	3579 ± 10	3403 ± 36
420	3079 ± 9	2881 ± 32
406	2567 ± 8	2431 ± 31
386	1903 ± 6	1796 ± 28
350	870 ± 1	932 ± 20
320	465 ± 3	

Table 4.3. Values of clusters light at different values of voltage applied to GEM1 and relative uncertainties. The results reported in table are obtained by studying data and MC. The voltage equal to 320 V was not simulated.

The plot 4.3 shows values of clusters light estimated by studying of data and MC events as functions of GEM1 HV. As we can note by looking the Figure 4.3 the results have a parallel trend. Both trends increase as the voltage applied to GEM1 increases. The results demonstrate the effectiveness of the developed algorithm also to simulate events with a reduced gain of the GEM stack, i.e. a lower amount produced charge. If we plot the light of clusters as function of particle energy we obtain a linear trend of light as the energy of particle travelling through the sensitive volume increases. The plot 4.4 shows how the light of clusters increases as the energy increases.

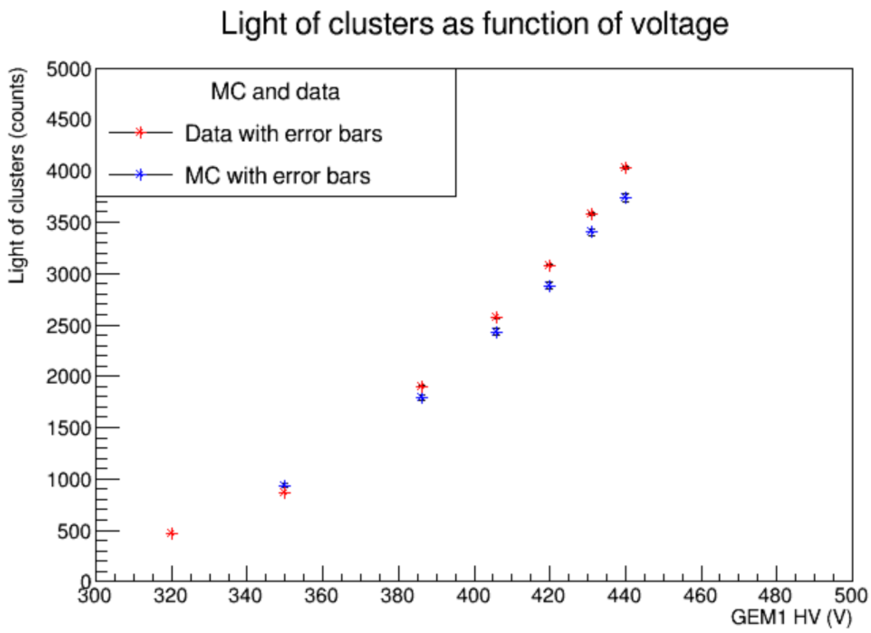

Figure 4.3. The picture shows the behaviors of data and MC as function of GEM1 voltage. The clusters light of both data and MC has a linear trend as the voltage of GEM1 changes.

Then, we estimated the size of clusters to study how it behaves as the voltage,

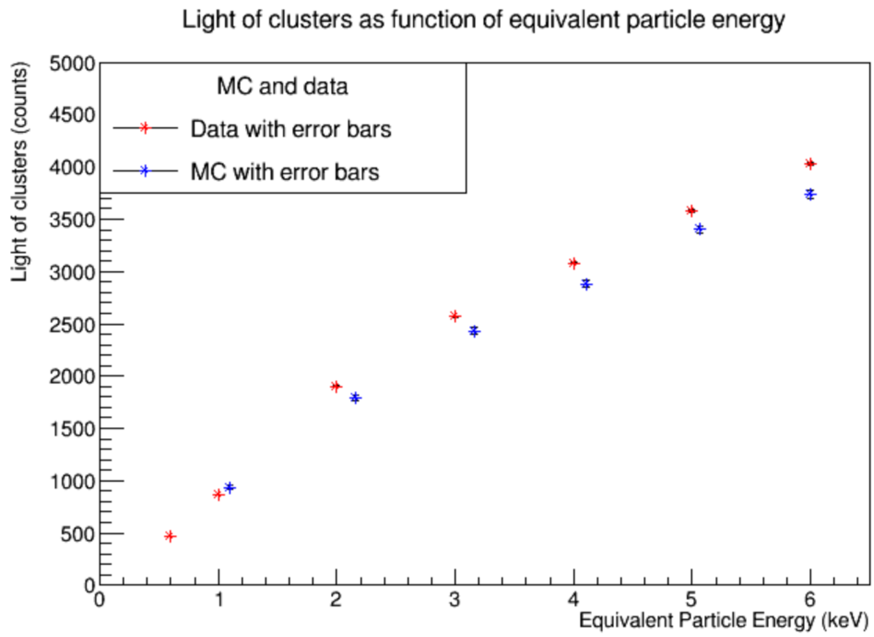

Figure 4.4. The plot shows clusters light obtained by data and MC as function of different values of energy. The behaviors are linear with the variation of energy.

such as the gain of GEM1, increases. The values of size obtained by the analysis of data and MC are reported in table 4.4. The size was estimated by counting the number of pixels composing clusters. The uncertainty associated with the corresponding size was obtained by fit of size distribution.

GEM1 HV (V)	s_{clu} ***of data (pixels)***	s_{clu} ***of MC (pixels)***
440	355.5 ± 0.6	431 ± 3
431	333.7 ± 0.5	416 ± 4
420	314.5 ± 0.5	373 ± 3
406	286.5 ± 0.5	356 ± 4
386	247.1 ± 0.4	313 ± 4
350	167.8 ± 0.4	234 ± 3
320	98.9 ± 0.4	

Table 4.4. Values of clusters size at different values of voltage applied to GEM1 and relative uncertainties. The results reported in table are obtained by studying data and MC. The voltage equal to 320 V was not simulated.

The Figure 4.5 shows the behavior of clusters size as function of GEM1 voltage.

The plot 4.5 shows the size increases with the voltage as we expected.

Finally, we compared the energy resolution estimated by analyzing both data and MC. The values obtained are reported in table 4.5. The table contains the energy resolutions obtained by data and MC. The uncertainties associated with the energy resolutions were estimated by the propagation of uncertainties. Then, we plotted these values as functions of GEM1 HV (Figure 4.6).

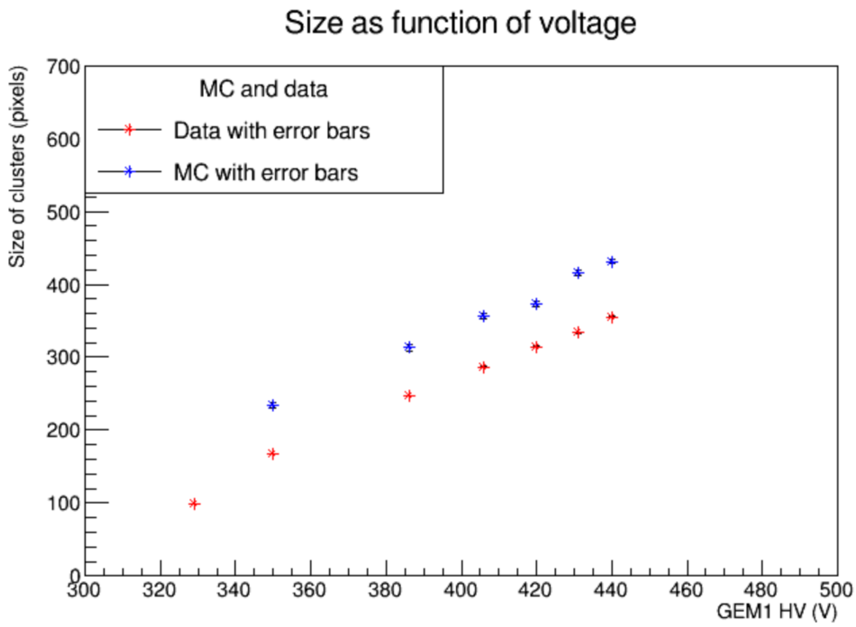

Figure 4.5. Behaviors of clusters size estimated by data and MC as function of voltage of GEM1. It seems the two behaviors to be parallel. The size of clusters increases as the voltage increases.

As the voltage increases the energy resolution decreases until it reaches an almost constant trend as we can note by looking the plot 4.6. In addition, data and MC results almost seem to coincide for any GEM1 HV value.

GEM1 HV (V)	R_{en} *of data*	R_{en} *of MC*
440	0.12 ± 0.02	0.11 ± 0.08
431	0.12 ± 0.02	0.11 ± 0.08
420	0.13 ± 0.02	0.11 ± 0.07
406	0.14 ± 0.02	0.12 ± 0.08
386	0.16 ± 0.02	0.15 ± 0.07
350	0.28 ± 0.01	0.22 ± 0.08
320	0.22 ± 0.04	

Table 4.5. Values of energy resolution at different values of voltage applied to GEM1 and relative uncertainties. The results reported in table are obtained by studying data and MC. The voltage equal to 320 V was not simulated.

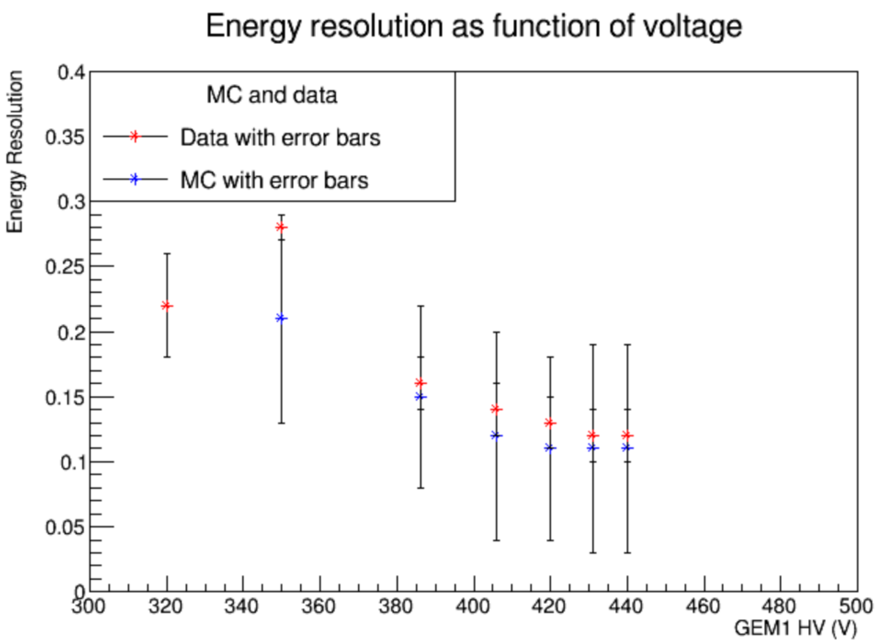

Figure 4.6. Behaviors of energy resolution obtained by data events and MC events. At low voltages R_{en} assumes higher values. At high voltages they decrease. At some values of GEM1 HV data and MC R_{en} appear coincident.

Chapter 5

Conclusions

The work of my thesis was to study the performances of LIME prototype before its underground installation at LNGS. I studied the dependence of light response as a function of the event position within the sensitive volume. Regarding the x and y coordinates, we saw that the light decreases as the distance from the centre of image increases. So, at higher values of x and y coordinates, that is at the edges of the cameras, the light assumes lower values. This effect is called vignetting effect. I tried to correct it to be able to study the light produced within the detector. After correcting the behavior of light as function of x and y coordinates, I studied the detector response for different positions of ^{55}Fe source, such as at different values of z. The results I obtained show that it increases as the distance of source from the GEM increases up to the position z = 25 cm where the light begins to decrease slightly. Instead, the energy resolution has an almost constant trend as function of z coordinate.
The next step of my work was to study the response of LIME detector as a function of the voltage applied to the first GEM. The reason of this study was to check if the detector was able to detect particles at lower energies. The results obtained by the analysis show that LIME detector is able to detect particles down to an equivalent energy of about 0.6 keV. So, the detector is a good candidate to detect DM particles and it is ready to be installed underground.
The experimental work was also important because it allowed us to validate the algorithm developed to simulate the detector response. By comparing data events and Monte Carlo events I obtained similar behaviors which allow us to consider the developed algorithm as reliable.
The study of dependence of light upon the three coordinates involved only runs with the first GEM at 440 V, while the study of capability of LIME to detect low energy particles involved runs corresponding to the source placed at z = 20 cm. In order to have a complete study of detector performances the same study is needed on other positions.
The experimental results are very encouraging. They indicate a good functioning on the whole volume and also at the low energies which are fundamental requirements for a DM detector that wants to explore low mass regions unexplored to date.

Bibliography

[1] A. Arbey and F. Mahmoudi, *Dark matter and the early Universe: a review*, In: *Progress in Particle and Nuclear Physics (2021) 103865*, arxiv:2104.11488

[2] F. Mayet, A. M. Green, J. B. R. Battar, J. Billard, N. Bozorgnia, G. B. Gelmini, P. Gondolo, B. J. Kavanagh, S. K. Lee, D. Loomba, J. Monroe, B. Morgan, C. A. J. O'Hare, A. H. G. Peter, N. S. Phan, and S. E. Vahsen, *A review of the discovery reach of directional Dark Matter detection*, In: *Physics Reports (2016)*, arXiv:1602.03781

[3] Annika H.G.Peter, Vera Gluscevic, Anne M. Green, Bradley J. Kavanagh, and Samuel K. Lee, *WIMP physics with ensembles of direct-detection experiments*, In: *Physics of the Dark Universe 5-6 (2014) 45-74*, arXiv:1310.7039

[4] F. D. Amaro, E. Baracchini, L. Benussi, S. Bianco, C. Capoccia, M. Caponero, G. Cavoto, A. Cortez, I. A. Costa, E. Dané, G. Dho, E. Di Marco, G. D'Imperio, F. Di Giambattista, R. R. M. Gregorio, F. Iacoangeli, H. Pessoa Lima Jùnior, A. da Silva Lopes Jùnior, G. Maccarrone, R. D. Passos Mano, M. Marafini, G. Mazzitelli, A. G. McLean, A. Messina, C. M. Bernardes Monteiro, R. A. Nobrega, I. F. Pains, E. Paoletti, L. Passamonti, S. Pelosi, F. Petruccci, S. Piacentini, D. Piccolo, D. Pierluigi, D. Pinci, A. Prajapaati, F. Renga, R. J. da Cruz Roque, F. Rosatelli, A. Russo, J. M. Ferreira dos Santos, G. Saviano, N. Spooner, R. Tesauro, S. Tomassini, and S. Torelli, *Directional Dark MAtter Searches with CYGNO*, In: *Particles (2021) 343-353*, https://doi.org./10.3390/particles4030029

[5] D. Pinci, *A triple-GEM detector for the muon system of the LHCb experiment*, Tech. rep. 2003

[6] S. Agostinelli, J. Allison, K. Amako, J. Apostolakis, H. Araujo, P. Arce, M. Asai, D. Axen, S. baneriee, G. Barrand, F. Behner, L. Bellagamba, J. Boudreau, L. Broglia, A. Brunengo, H. Burkhardt, S. Chauvie, J. Chuma et al., *GEANT4-a simulation toolkit*, In: *Nuclear Instruments and Methods in Physics Research Section A: Accelerators, Spectrometers, Detectors and Associated Equipment (2003) 250-303*, https://doi.org/10.1016/S0168-9002(03)01368-8

[7] *ORCA-Fusion Digital CMOS camera: C14440-20UP*, https://www.hamamatsu.com/eu/en/product/cameras/cmos-ccameras/index.html

[8] Hubble time, https://www.oxfordreference.com/view/10.1093/oi/authority.20110803095948568

[9] L. Rolandi, W. Riegler, and W. Blum, *Particle Detection with Drift Chambers*, Springer, Berlin, Heidelberg, 2008

[10] Fraga, M. M. F. R. and Fraga, F. A. F. and Fetal, S. T. G. and Margato, L. M. S. and Ferreira-Marques, R. and Policarpo, A. J. P. L, *The GEM scintillation in He CF-4, Ar CF-4, Ar TEA and Xe TEA mixtures*, In: *Nucl. Instrum. Meth. A (2003) 504*, 0.1016/S0168-9002(03)00758-7

[11] W. Emery and A. Camps, *Introduction to Satellite Remote Sensing*, Elsevier, 2017, https://www.sciencedirect.com/science/article/pii/B9780128092545000038

[12] Marafini et al., *IEEE TRANSACTIONS ON NUCLEAR SCIENCE*, VOL.65, NO.1, JANUARY 2018

[13] V.C. Antochi, E. Baracchini, G. Cavoto, E. Di Marco, M. Marafini, G. Mazzitelli, D. Pinci, F. Renga, S. Tomassini, and C. Voena, *Combined readout of a triple-GEM detector*, In: *Journal of Instrumentation (2018) JINST 13 P05001*, https://doi.org/10.1088/1748-0221/13/05/p05001

[14] S. E. Vahsen and others, *CYGNUS: Feasibility of a nuclear recoil observatory with directional sensitivity to dark matter and neutrinos*, arXiv:2008.12587v2

[15] K. Miuchi, and E. Baracchini, and G. Lane, and N. J. C. Spooner, and S. E. Vahsen, *CYGNUS*, In: *J. Phys. Conf. Ser (2020) 1468*, 10.1088/1742-6596/1468/1/012044